ENG. Struct. Civ. Eng. 2026, 20(4): 781–803
https://doi.org/10.1007/s11709-026-1287-7

RESEARCH ARTICLE

Fragility and recoverability assessment of single-tower cable-stayed bridge under near-fault impulsive ground motion

Jin ZHANG[a*], Zhong-yao ZHANG[a], Gao ZHANG[a,b]

[a] *College of Environment & Civil Engineering, Chengdu University of Technology, Chengdu 610059, China*
[b] *School of Civil Engineering, Central South University, Changsha 410075, China*
[*] *Corresponding author. E-mail: zhangjin18@cdut.edu.cn*

ABSTRACT This study examines the seismic performance and post-earthquake recoverability of cable-stayed bridges, with the Tianhekou Bridge adopted as a prototype. A refined finite element model was established, and nonlinear dynamic analyses were performed using ground motion records from the pacific earthquake engineering research center (PEER)database. The objectives were to assess site amplification effects, compare responses under impulsive and non-impulsive excitations, and quantify structural vulnerability and recoverability. The results show that: 1) the site effects markedly amplify peak ground acceleration (PGA) and alter waveform characteristics, thereby increasing seismic demand; 2) transverse displacements exceed longitudinal responses, with impulsive motions producing the largest deformations, including a maximum of 0.35 m at pier 4#; 3) vulnerability analysis reveals that the probability of severe damage in bearing 2# increases with PGA, reaching 84.65% at 1.0*g*; and 4) recoverability assessment indicates that the bearing system has the highest restoration potential (index = 0.645), while the main girder system has the lowest (index = 0.282). These findings provide a basis for enhancing the seismic resilience of cable-stayed bridges.

KEYWORDS cable-stayed bridge, site effect, bridge collapse, fragility analysis, recoverability analysis

1 Introduction

In recent years, the response to bridges, especially cable-stayed bridges, caused by ground motion induced by near-fault effects has attracted much attention [1–3]. Cable-stayed bridges are favored for their aesthetic appeal, large spans, and robust bearing and seismic capacities [4–8]. However, intricate structural design leads to a complex distribution of internal forces during seismic events. Notably, the response of single-tower cable-stayed bridges is particularly sensitive, highlighting the importance of conducting thorough seismic analyses.

Near-fault earthquakes, occurring near active faults, exhibit high intensity and are classified as impulsive or non-impulsive. Both types combine high-frequency and long-period content, but impulsive earthquakes are further distinguished by strong velocity pulses, necessitating enhanced fatigue and seismic resistance in bridges [9,10]. Guo et al. [11] simulated artificial impulsive ground motions using a combination of high- and low-frequency methods. Their results indicated that the transition pier bearing is the most susceptible to damage. Franchini et al. [12] analyzed the damage mechanism of cable-stayed bridges using computer simulations, an approach that significantly reduces construction costs. Variyavwala et al. [13] investigated the probability of damage of cable-stayed bridges under different bridge types by using a variety of tower types. To study bridge damage under different site conditions, Zhong et al. [14] evaluated cable-stayed bridge components under marine earthquakes. Their results showed that the damage states (DS) of these components were significantly more severe than those of their counterparts under land earthquakes. Jiao et al. [1] conducted a fragility analysis of a 6-tower cable-stayed bridge. Currently, most of the fragility analysis has been

Article history: Received Aug 25, 2025; Accepted Nov 5, 2025

conducted on twin and multi-tower cable-stayed bridges, and very few studies have been conducted on single-tower cable-stayed bridges.

Near-fault pulse ground motions significantly impact the key seismic responses of cable-stayed bridges. Research by Jia et al. [15,16] demonstrated that for bridges with main spans of 680 and 432 m, these motions cause more severe structural damage and amplify displacement responses two to three times over far-field motions. Bidirectional peak ground velocity (PGV) is a critical influencing parameter, and the directional effect is particularly pronounced. Similarly, Gao et al. [17] found that long-period pulses considerably affect bridges supported by high piles. To enhance seismic performance, novel damping and isolation systems have been developed, such as a horizontal bidirectional hybrid damping system and an elastoplastic cable-fluid viscous damper (FVD) lateral isolation system [18,19]. Significant advancements have also occurred in simulation and analysis methods. Xu et al. [20] combined an incremental dynamic analysis (IDA)-based prediction model with the endurance time analysis (ETA) method, achieving about 10% average prediction error and overcoming ETA's limitations. Yi et al. [21] showed that multi-segment cable modeling is necessary, as traditional single truss elements overestimate responses. Together with methods like direct probability integral method (DPIM) for random motions [22], these improvements have boosted the accuracy of near-fault seismic assessments.

In previous studies, bridge collapse has been extensively investigated by different scholars. Lin et al. [23] based on numerical twin calculations concluded that choosing the appropriate intensity measure (IM) metrics is important for bridge collapse assessment. Zheng et al. [24] established a progressive bridge collapse framework. Scattarreggia et al. [25] conducted a frame-by-frame comparison between numerical simulations and the actual bridge collapse process to evaluate strength prediction methods. Their analysis demonstrated that although the analytical method requires significant simplification, it can still produce reasonable strength estimates compared to the finite element method. The current ability to analyze the collapse process of bridges in an earthquake is still limited, especially the full bridge collapse analysis of large cable-stayed bridges needs to be strengthened.

Previous studies have extensively explored post-earthquake recoverability. Scattarreggia et al. [26] proposed a rapid post-earthquake accessibility assessment method for cable-stayed bridges based on Latin hypercube sampling and IDA. Qian et al. [27] evaluated the lifetime resilience of steel-shape memory alloy (SMA) reinforced concrete bridges by considering random ground motions and functional deterioration. Chandrasekaran et al. [28] employed a multi-objective optimization algorithm to enhance retrofit solutions for post-earthquake assessments, focusing on multi-hazard resilience and retrofit costs. Additionally, Badroddin et al. [29] developed a probabilistic resilience assessment framework for simply supported bridges under scenarios of seismic activity, scour, and environmental degradation. Collectively, the seismic recoverability of cable-stayed bridges has been extensively studied; however, their performance under near-fault impulsive ground motions has received comparatively little attention. There are notable discrepancies among different disaster types regarding disaster probability and structural fragility analysis, indicating that the existing theoretical framework for bridge seismic research is incomplete. Therefore, it is imperative to enhance the theoretical framework for seismic analysis of bridges.

LS-DYNA finite element software is widely utilized for numerical simulations in civil engineering due to its extensive material library and robust capability to model real structures [30,31]. Agalianos et al. [32] established the interaction relationship between axial force, bending moment, shear force, and torque in concrete piers under impulsive seismic action. Separately, Hu et al. [33] realized simplified coupling of rigid surfaces between solid beams, while Jia et al. [34] derived that large-span continuous girder bridges with fixed pier bottoms primarily undergo bending plastic damage under ground motion. Currently, LS-DYNA is predominantly used for the solid analysis of small bridges and various material types in fundamental analyses. However, comprehensive damage analysis of complex bridge structures has not yet been conducted. By utilizing LS-DYNA for solid modeling and incorporating nonlinear material functions and property definitions, it is possible to realistically simulate the DS and processes of bridges under seismic actions. This capability is crucial for identifying damaged components of the bridge and for planning subsequent repair strategies, thereby significantly contributing to the assessment and restoration of bridge integrity post-earthquake.

This study investigates the effects of near-fault impulsive and non-impulsive ground motions on a typical single-tower cable-stayed bridge. A nonlinear finite element model was developed by transferring the ANSYS APDL code to an LS-DYNA keyword program to incorporate material nonlinearity. Natural ground motions selected from the pacific earthquake engineering research center (PEER) database were applied to the model using a multi-point excitation method. After that, the whole bridge collapse mechanism of cable-stayed bridges under strong seismic effects is investigated. Then, the damage-prone parts of the bridge are identified after the dynamic response analysis, and the damage assessment of the bridge structure is carried out through the fragility analysis. Finally, based on the proposed recoverable model, the most vulnerable parts of the bridge are

analyzed for post-earthquake recoverability. This study provides theoretical guidance for LS-DYNA modeling, seismic design, and damage analysis of cable-stayed bridges under near-fault earthquakes. The specific flow of this paper is shown in Fig. 1.

2 Bridge model

2.1 Bridge structure

The single-tower cable-stayed bridge has a total length of 373 m with span arrangement of (222 + 70 + 40 + 41) m and a main tower height of 260.5 m. The cross-sectional dimensions of the piers are as follows: pier 1# measures 4 m × 4 m; piers 2# and 3# share identical dimensions of 4 m × 2.5 m; and pier 4# measures 4 m × 3.6 m. The pier is connected with the main girder with the use of fixed rubber bearings (bearing 1# is 870 mm × 870 mm × 235 mm, bearings 2#–4# is 770 mm × 770 mm × 232 mm). The main girder is made of C50 concrete, the pier and the main tower are made of C40 concrete, and the pier rebars are made of HRB360 with a diameter of 0.028 m. The cable ties are made of steel wire bundles, and the cable ties are arranged as double-sided cables, with each side of the cable face consisting of 24 pairs of cable ties. Each pier, bearing, main girder name and layout details are shown in Fig. 2.

2.2 Finite element model of the bridge

As shown in Fig. 3, the main coordinate system is defined

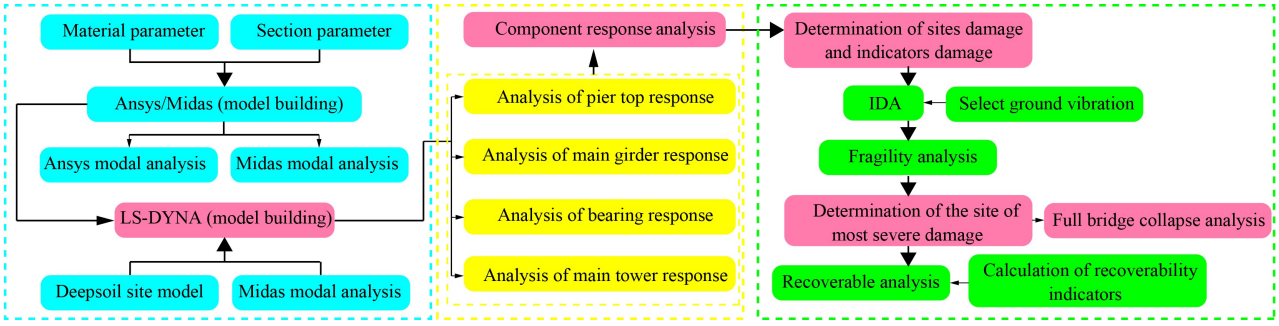

Fig. 1 Schematic diagram of the component response and damage assessment framework of a single-tower cable-stayed bridge under a near-fault impulsive earthquake.

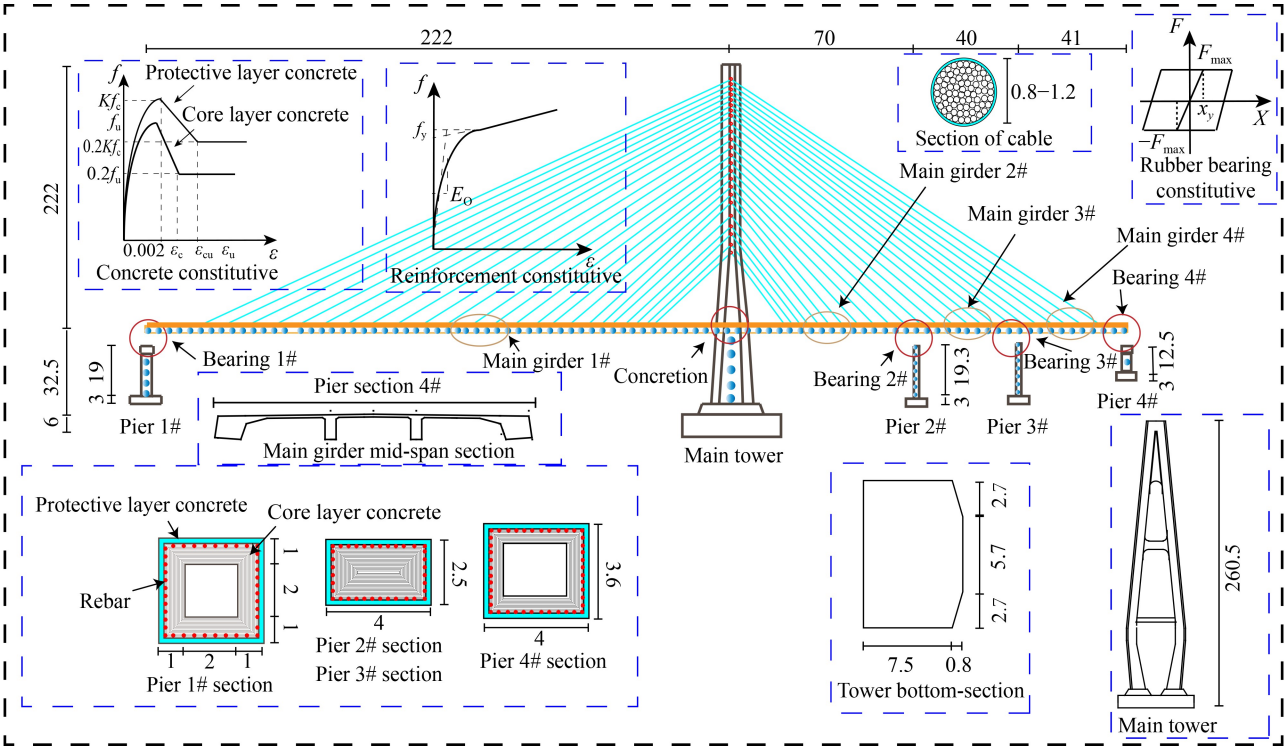

Fig. 2 The layout of single-tower cable-stayed bridge (unit: mm). (Note: Define pier 1# and pier 4# as side piers, pier 2# and pier 3# as center piers.)

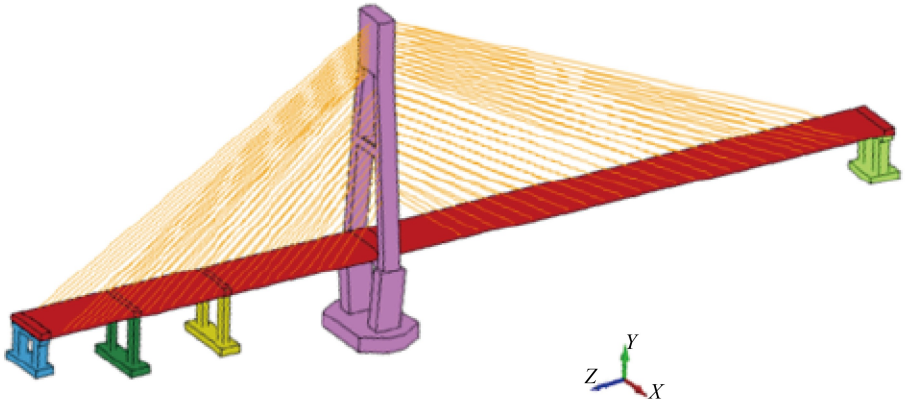

Fig. 3 LS-DYNA finite element model.

with the *X*-axis in the transverse direction, the *Y*-axis in the vertical direction, and the *Z*-axis in the longitudinal direction. The main girders, bearings, piers and main towers are simulated by solid cells (SOLID164), and the rebars and diagonal cables are simulated by beam cells (BEAM161). Due to the large overall structure of the bridge, the grid division size is larger, the pier grid size is 1.0 m, the main girder grid size is 2.0 m, the bearing grid size is 0.1 m, the main tower and the main girder contacting part of the grid size is 1.0 m, and the other parts are 2.0 m (for the sake of calculation convenience, only 4 piers are reinforced). Table 1 shows the detailed information of the material model and parameters of the single-tower cable-stayed bridge in this paper.

The piers and main girders are modeled using the *MAT_CSCM_CONCRETE(MTA_159) material model, which not only automatically generates other parameters and simulates various complex behaviors of concrete based on the provided unconfined compressive strength, but also takes into account the viscoplastic stresses of the material:

$$\sigma_{ij}^{\mathrm{vp}} = (1-\gamma)\sigma_{ij}^{\mathrm{T}} + \gamma\sigma_{ij}^{\mathrm{P}}, \tag{1}$$

$$\gamma = \frac{\Delta t/\eta}{\Delta t/\eta + 1}, \tag{2}$$

where $\sigma_{ij}^{\mathrm{vp}}$ is the viscoplastic stress, σ_{ij}^{T} is the elastic stress, σ_{ij}^{P} is the non-viscous stress, η is the effective flow coefficient, and Δt is the unit time step.

The rebars and diagonal cables are modeled using the *MAT_PLASTIC_KINEMATIC material model. This model simulates the elastic-plastic behavior of the rebar and efficiently captures the reinforcement hardening. It also accounts for the strain rate sensitivity to determine the yield stress:

$$\sigma_y = \left[1 + \left(\frac{\dot{\varepsilon}}{C}\right)^{\frac{1}{P}}\right](\sigma_0 + \beta E_{\mathrm{p}}\varepsilon_{\mathrm{eff}}^{\mathrm{p}}), \tag{3}$$

where σ_0 is the initial yield stress, $\dot{\varepsilon}$ is the strain rate, $\varepsilon_{\mathrm{eff}}^{\mathrm{p}}$ is the effective plastic strain, β is the hardening parameter, E_{p} is the plastic hardening modulus, C and P are the strain rate parameters.

2.3 Bridge model analysis

Comparing the modal of MIDAS and ANSYS, (the beam unit in LS-DYNA cannot be analyzed implicitly dynamic analysis, so this paper carries out the modal analysis of the ANSYS bridge model before converting the K file). From Table 2, it can be seen that the first 6 orders of vibration modes mainly show the vertical bending of the main girder and the transverse bending of the main tower, and it can be found that the vertical direction of the bridge shows obvious flexible characteristics. The comparison shows that the frequencies obtained from MIDAS and ANSYS are basically the same, which proves that the model has high accuracy. Figure 4 shows the schematic diagram of the first six-order vibration modes of the bridge.

3 Generation of ground motion at the site and bridge response analysis

3.1 Selection of ground motion

The bridge site is located in a seismically active zone with multiple faults at distances ranging from 6 to 12 km. Following the Class II site classification specified in China's "Code for Seismic Design of Buildings" (GB50011-2010), and based on fault distances and ground motion characteristics, one near-fault impulsive ground motion record (Duzce, Turkey) and one near-fault non-impulsive record (Loma Prieta) were selected from the PEER database. The detailed information of the selected ground motions is presented in Table 3.

To simulate the ground motion representative of the actual site conditions, the multiple-degree-of-freedom (MDOF) set total mass system is used through DEEPSOIL nonlinear site response analysis modeling

Table 1 LS-DYNA single-tower cable-stayed bridge material model and parameters

Type	Material model	Material parameter	Value	Refs.
Main tower, pier	*MAT_CSCM_CONCRETE	mass density (kg/m^3)	2300	[35–37]
		compressive strength (MPa)	40	
		maximum aggregate size (mm)	25	
		IRATE	1.0	
		RECOV	0.5	
		ERODE	1.075	
Main girder	*MAT_CSCM_CONCRETE	mass density (kg/m^3)	2300	[35–37]
		compressive strength (MPa)	50	
		maximum aggregate size (mm)	25	
		IRATE	1.0	
		RECOV	0.5	
		ERODE	1.075	
Rebar	*MAT_PLASTIC_KINAMATIC	mass density (kg/m^3)	7800	[38–40]
		yield stress (MPa)	400	
		Young's modulus (GPa)	200	
		C (strain rate parameter)	40.4	
		P (strain rate parameter)	5	
		failure strain	0.12	
Diagonal cable	*MAT_PLASTIC_KINAMATIC	mass density (kg/m^3)	7800	[38–40]
		yield stress (MPa)	1860	
		Young's modulus (GPa)	200	
		C (strain rate parameter)	40.4	
		P (strain rate parameter)	5	
		failure strain	0.12	
Bearing	*MAT_VISCOELASTIC	mass density (kg/m^3)	2300	[41]
		elastic bulk modulus (MPa)	6820	
		short-time shear modulus (MPa)	8.35	
		long-time shear modulus (MPa)	17.32	

Table 2 Modal details of bridges with different finite element software

Order	Frequency		Error (%)	Model
	LS-DYNA	MIDAS		
1	0.59415	0.58976	0.74	main girder side span positive symmetrical vertical bending
2	0.85604	0.88394	3.16	main tower transverse bending
3	0.99438	1.00729	1.28	main girder side span anti-symmetric vertical bending
4	1.0794	1.21824	11.40	main girder side span torsion
5	1.3858	1.33212	4.03	main girder side span positive symmetrical vertical bending
6	1.4874	1.43257	3.83	main girder side span anti-symmetric torsion

software, in addition, the dynamic equilibrium equations are solved numerically using the Newmark method [42,43].

The nonlinear eigen-structural model used in this paper is based on the matasovic-kavazanjian-zhao (MKZ) model with Hashash and Park [42,43] optimizing the model strain parameters:

$$\gamma_{\mathrm{r}} = a\left(\frac{\sigma_{\mathrm{v0}}}{\sigma_{\mathrm{ref}}}\right)^{b}, \tag{4}$$

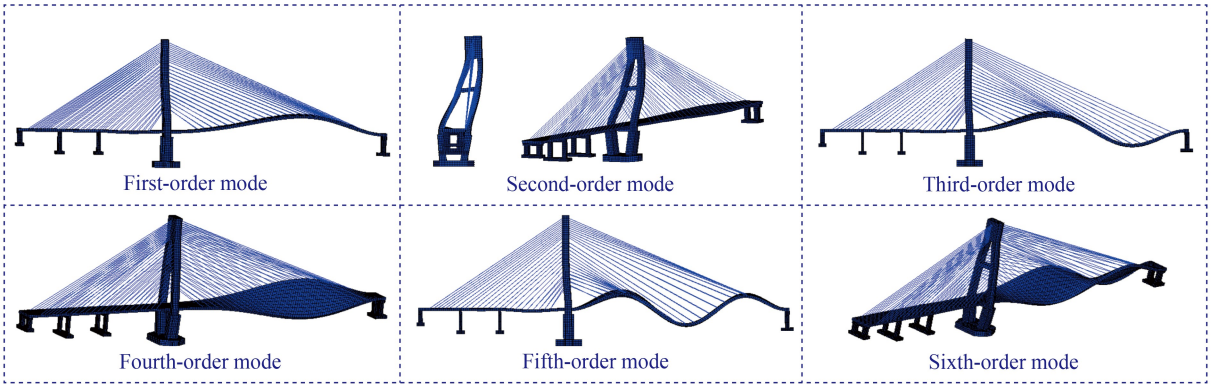

Fig. 4 Bridge modal.

Table 3 Selected ground motion information

Ground motion	Station	Grade	Year	A_p/V_p	V/H	Fault distance (km)	Vs_{30} (m/s^2)
Duzce-Turkey (DZC)	Duzce	7.14	1999	6.11	0.67	6.58	281
Loma-Prieta (BRN)	Bran	6.93	1989	8.88	1.10	10.72	476

where γ_r is the shear strain, σ_{v0} and σ_{ref} represent the effective vertical stress and reference perimeter pressure, respectively, a, b are the curve-fitting parameters of the initial backbone curve.

Derive the equation for the hysteresis curve in DEEPSOIL:

$$\tau = \frac{G_{M0}\gamma}{1+\alpha\left(\frac{\gamma_r}{\gamma}\right)^s}, \tag{5}$$

where τ is the shear stress, G_{M0} is the initial shear modulus; α and s are the initial principal curve fitting coefficients.

The soil layers at a bridge site are, in descending order from the ground surface, miscellaneous fill, chalk, chalky sand, fine sand, chalky clay, chalk, fine sand, Powdered clay, weathered rock, etc.; detailed soil layer profiles are shown in Table 4 (Note: shear wave speeds of more than 500 m/s^2 can be defined as bedrock).

The selected ground motion records were processed through the DEEPSOIL model to simulate their propagation through the local site conditions. Figure 5 presents the resulting near-fault impulsive and non-impulsive ground motions at the surface level. Compared to the bedrock input motions, significant modifications in the acceleration time histories are observed. Besides the expected amplification of the peak ground acceleration (PGA), the surface motions exhibit a pronounced increase in spectral intensity, with the peak acceleration at the surface layer being substantially larger than that at the bedrock level.

Figure 6 illustrates the variation of PGA as seismic waves propagate through different soil layers. The analysis reveals a consistent amplification pattern for both impulsive and non-impulsive ground motions across the soil profile: PGA initially increases, then decreases, followed by another increase. The most significant amplification occurs in soil layer 2. Interestingly, even within the same soil type, different layers demonstrate

Table 4 Bridge site soil parameters

No.	Soil thickness (m)	Shear-wave velocity (m/s)	Soil description
1	0.6	270	miscellaneous fill: multi-colored mix, loosely distributed, mostly construction debris
2	1.9	152	chalk: pale yellow, slightly moist, dense
3	3.5	295	chalky sand: yellow, rounded, moderately dense, slightly wet
4	2.2	215	fine sand: yellow, rounded, medium dense, medium wet
5	3.1	229	chalky clay: yellowish brown, slightly moist, with soft plasticity
6	1.2	274	chalk: yellowish gray, dense, moist
7	3	282	fine sand: yellow, round-grained, dense, moist
8	13.2	316	powdered clay: yellowish brown, moist, dense, strongly plastic
9	8.5	844	weathered rock: gray, looser rock, metamorphic structure
10	–	1500	granite: gray-black, high rock hardness, metamorphic, gneiss-like structure

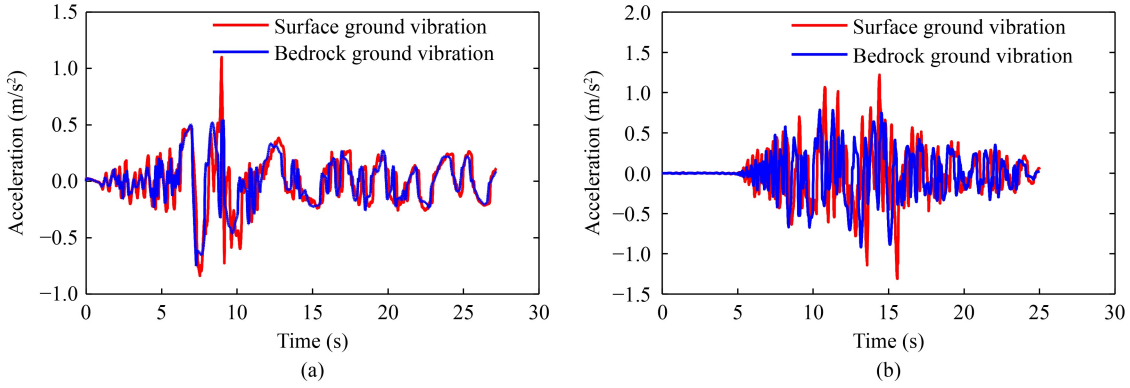

Fig. 5 Site ground motion model based on DEEPSOIL software: (a) DZC-ground motion; (b) BRN-ground motion.

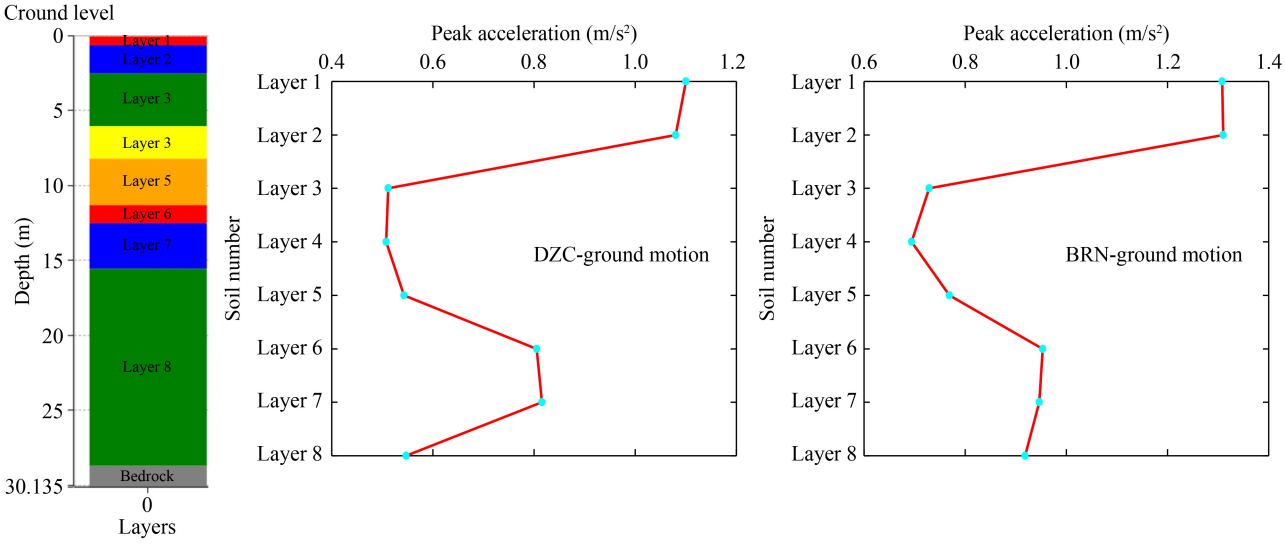

Fig. 6 Peak acceleration for different soil layers.

varying amplification effects. For example, although both layer 2 and layer 6 are classified as chalk, their distinct densities and shear wave velocities result in markedly different influences on seismic wave propagation.

The PGA for the ground motion is set to four distinct levels: 0.7 m/s^2 (multiple ground motion), 1.5 m/s^2 (design ground motion), 3.1 m/s^2 (rare ground motion), and 6.25 m/s^2 (megathrust ground motion), as shown in Fig. 7.

The frequency content of ground motions can be characterized using Fourier transform techniques, which convert acceleration time histories into Fourier amplitude spectra in the frequency domain. The fast fourier transform algorithm is employed to efficiently compute the discrete Fourier transform. This process decomposes complex signals into simple harmonic components with distinct frequencies, amplitudes, and phases, thereby revealing dominant frequencies and energy distribution characteristics. Figure 8 presents the Fourier amplitude spectra and corresponding time-domain acceleration responses for multiple signals, including pulse-like (D) and non-pulse-like (B) ground motions, providing critical insights into their spectral features and dynamic behaviors.

Clear spectral patterns are observed in the frequency domain. Both pulse-like signal D1 and non-pulse-like signal B1 show high Fourier amplitudes below approximately 20 Hz, with gradual amplitude decay at higher frequencies. This indicates dominant low-frequency components in their dynamic responses. In comparison, signals D2 and B2 exhibit similar spectral shapes but with significantly lower amplitude levels across all frequencies, suggesting weaker energy content. The Fourier amplitudes of D3, B3, D4, and B4 are further reduced, with energy concentrated primarily in the very low-frequency range, indicating both lower intensity and narrower effective bandwidth.

The time-domain responses correlate well with these spectral characteristics. Records D1 and B1 display the most pronounced acceleration fluctuations, consistent with their strong low-frequency spectral content and indicating potentially significant structural dynamic responses. The oscillations of D2 and B2 are substantially milder, matching their reduced spectral amplitudes. The

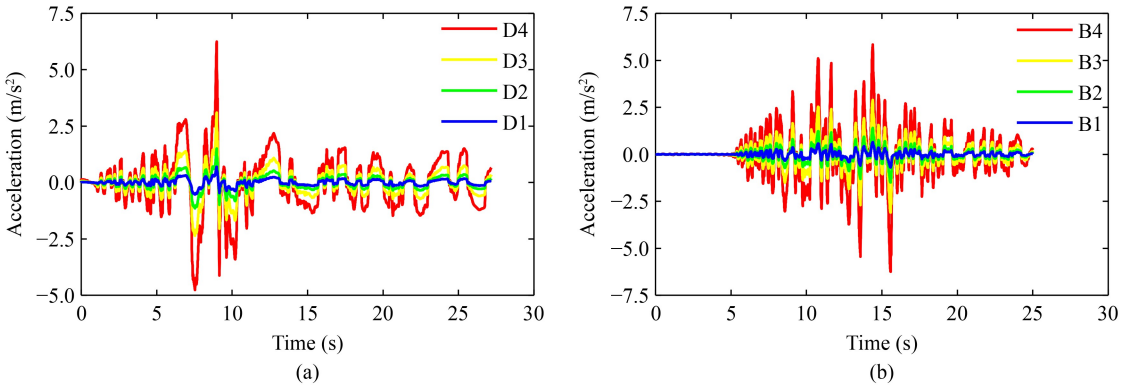

Fig. 7 Adjusted acceleration time history: (a) DZC-ground Motion; (b) BRN-ground Motion. (Note: The conditions are defined as follows: DZC ground motion with PGA = 0.7 m/s^2 corresponds to condition D1; PGA = 1.5 m/s^2 corresponds to condition D2; PGA = 3.1 m/s^2 corresponds to condition D3; and PGA = 6.25 m/s^2 corresponds to condition D4. The BRN ground motion is categorized in a manner analogous to that of the DZC ground motion.)

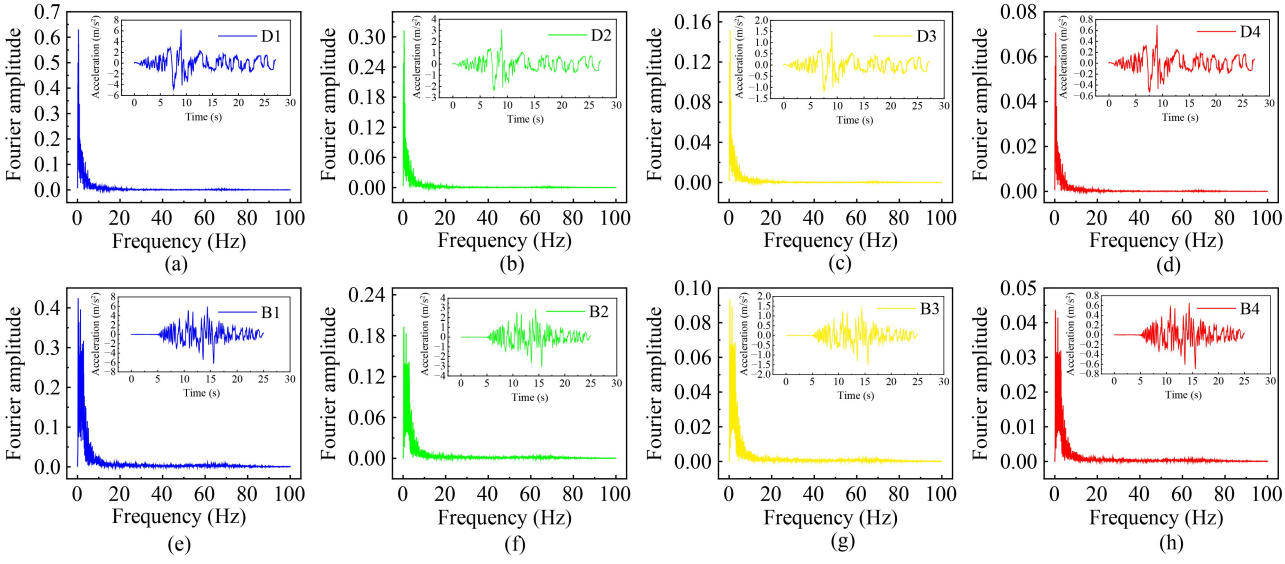

Fig. 8 Comparison of Fourier amplitude spectra under different accelerations: (a) D1 ground motion spectrum; (b) D2 ground motion spectrum; (c) D3 ground motion spectrum; (d) D4 ground motion spectrum; (e) B1 ground motion spectrum; (f) B2 ground motion spectrum; (g) B3 ground motion spectrum; (h) B4 ground motion spectrum.

acceleration time histories of D3, B3, D4, and B4 show the smoothest patterns with minimal variations, directly confirming their low spectral amplitudes and collectively demonstrating weak dynamic excitation and subdued structural responses.

We selected two representative sets of pulse-like and non-pulse-like ground motions. This selection followed a preliminary analysis of 30 records with diverse characteristics. The analysis showed that while different ground motions caused variations in absolute response values, the trends in key structural parameters were stable and consistent. Therefore, using representative records allows us to clearly demonstrate the proposed analytical framework and reveal the core response patterns.

3.2 Analysis of bridge member response

As can be seen from Fig. 9, with the increase of seismic intensity, the displacement of the top of each pier shows an increasing trend. Notably, the impulsive seismic displacement response is much larger than that of non-pulse seismic, for example, in the longitudinal direction of pier 1#, the displacement peaks in D1–D4 are: 0.024, 0.051, 0.102, 0.201 m; displacement peaks in B1–B4 are: 0.006. 0.013, 0.029, 0.044 m.

Under impulsive earthquake action, the longitudinal and transverse displacements at the top of each pier follow a consistent pattern: the side piers (piers 1# and 4#) exhibit larger displacements, while the intermediate piers (piers 2# and 3#) experience relatively smaller displacements. It is noteworthy that the transverse displacement increases most significantly from pier 3# to 4#, with a peak displacement surge of 289%. This substantial increase in displacement demands particular attention in practical engineering applications.

In the non-impulsive earthquake, the longitudinal

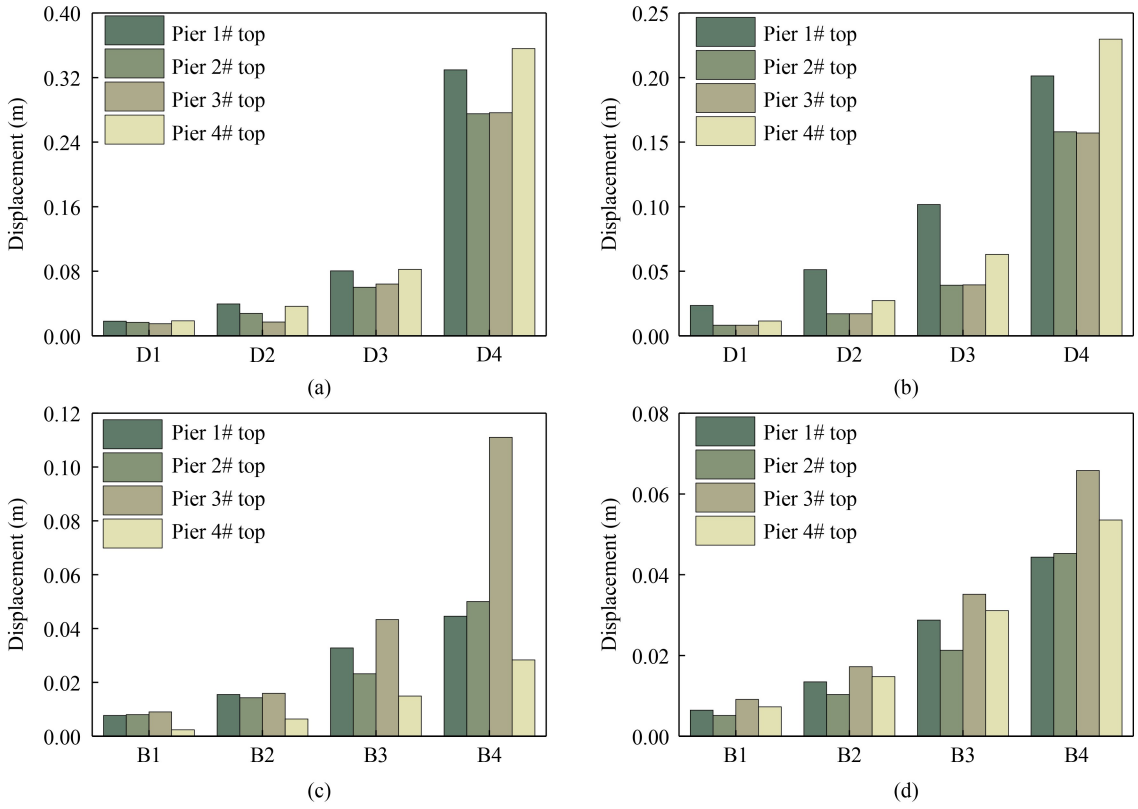

Fig. 9 Comparative study of pier top displacements induced by impulsive versus non-impulsive seismic records: (a) transverse components for impulsive records; (b) longitudinal components for impulsive records; (c) transverse components for non-impulsive records; (d) longitudinal components for non-impulsive records.

(transverse) displacement of each pier top is the largest for pier 3#, it is worth noting that, from B3 to B4, pier 3# transverse displacement increased by 144%, the displacement increase is the most significant, but the increase in displacement is only 0.11 m, the impact effect on the pier is not large.

Integrated analysis reveals distinct seismic response patterns in the single-pylon cable-stayed bridge (with rigid tower-girder connections) under impulsive versus non-impulsive ground motions. Under non-impulsive excitations, the structural behavior is primarily governed by fundamental vibration modes, generally resulting in larger displacements at intermediate piers than at side piers in both transverse and longitudinal directions, albeit with occasional exceptions. In contrast, near-fault impulsive motions, characterized by high-energy, long-period velocity pulses, significantly excite higher-order vibration modes. This shifts the displacement pattern, amplifying responses at side piers and even causing them to exceed those at intermediate piers, indicating a transition in damage mechanisms. Furthermore, the long-period components of impulsive motions readily induce resonant effects with the fundamental period of the bridge, while the intense energy input within a short duration forces the structure to dissipate energy through pronounced nonlinear deformations. Collectively, these mechanisms lead to consistently and substantially larger pier-top displacements under impulsive motions compared to non-impulsive motions across all cases.

The peak mid-span displacements of each main girder are shown in Fig. 10, from which it can be seen that the mid-span displacements of the main girder under impulsive seismicity are much larger than those under non-impulsive seismicity; moreover, the longitudinal (transverse) displacements of each main girder under impulsive and non-impulsive seismicity are basically the same in each condition, and the largest difference is that the longitudinal displacements of the main girder in the mid-span of the main girder 2# and the main girder 3# under D3 are different by 0.02 m, which is in the range of main girder's capacity to withstand.

The bearing is the connecting member of the pier and the main girder, which is significantly affected by the earthquake, and it can be seen from Fig. 11 that the displacement of the bearing under the impulsive earthquake is much larger than that of the non-pulse earthquake, for example, the longitudinal displacements of the bearing 1# from D1 to D4 are: 0.015, 0.034, 0.065, and 0.118 m; and from B1 to B4, the displacements are: 0.005, 0.011, 0.023, and 0.042m. In addition, under the longitudinal earthquake, the displacement of bearing 1# is much larger than the other bearings; however, under the transverse earthquake, when the PGA is small, it presents the law that the displacements of bearings 2# and 3# are

large, and the displacements of bearings 1# and 4# are small; and when the ground motion is large, it presents a completely opposite law. The response reversal of bearings 2# and 3# is due to a shift in seismic force distribution. Their larger response under weak motions results from the lower transverse stiffness of their supporting piers. Under strong motions, plastic hinge formation at the tower base redistributes forces to stiffer members, reducing the relative load on bearings 2# and 3#.

The displacement time histories of the main tower top under different conditions are extracted and shown in Fig. 12. As observed in Figs. 12(a) and 12(b), the peak tower top displacement coincides with the impulsive peak of the ground motion. From conditions D1 to D4, the longitudinal displacement peaks are 0.01, 0.02, 0.05, and 0.10 m, while the transverse displacement peaks are 0.01, 0.03, 0.05, and 0.11 m, respectively. This indicates that the transverse displacement is larger than the longitudinal

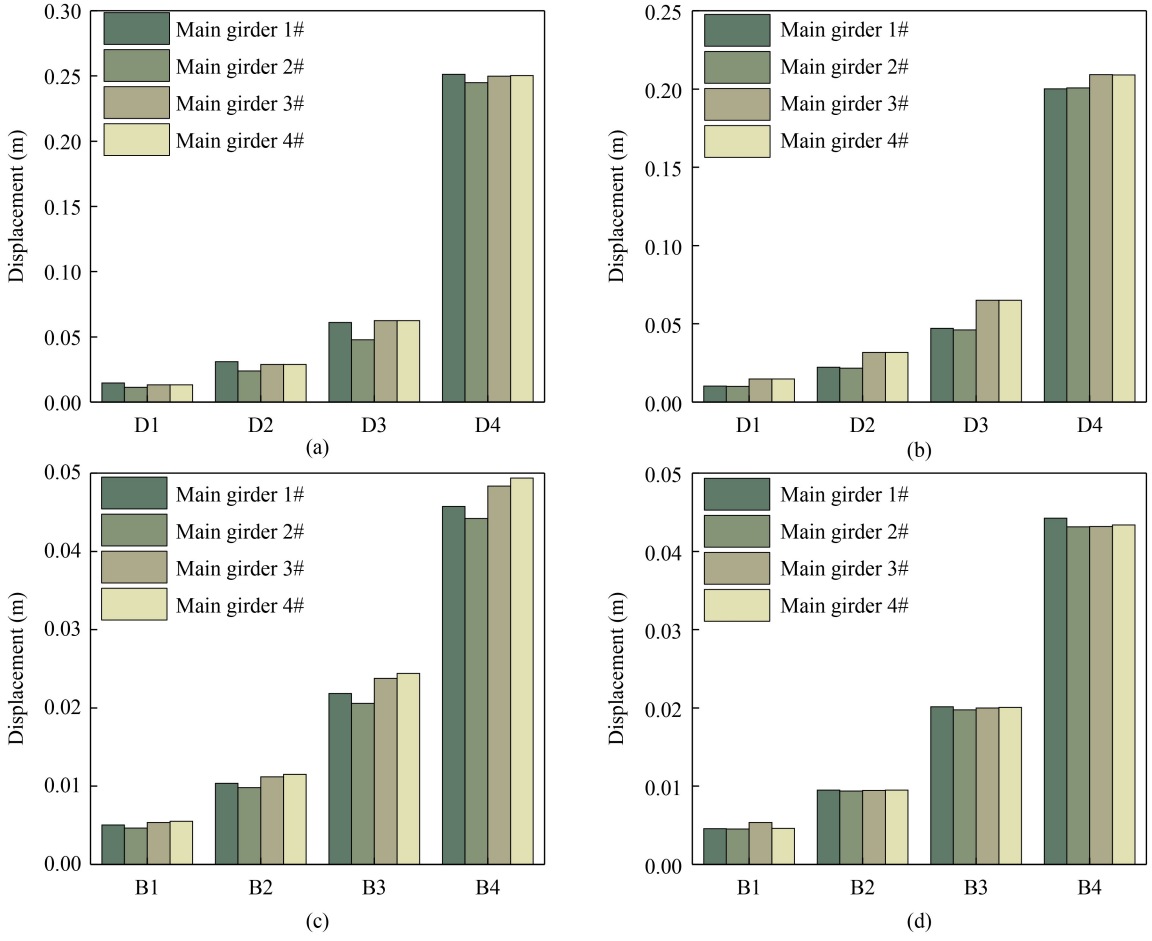

Fig. 10 Comparative study of displacements in the main girder span induced by impulsive versus non-impulsive seismic records: (a) transverse components for impulsive records; (b) longitudinal components for impulsive records; (c) transverse components for non-impulsive records; (d) longitudinal components for non-impulsive records.

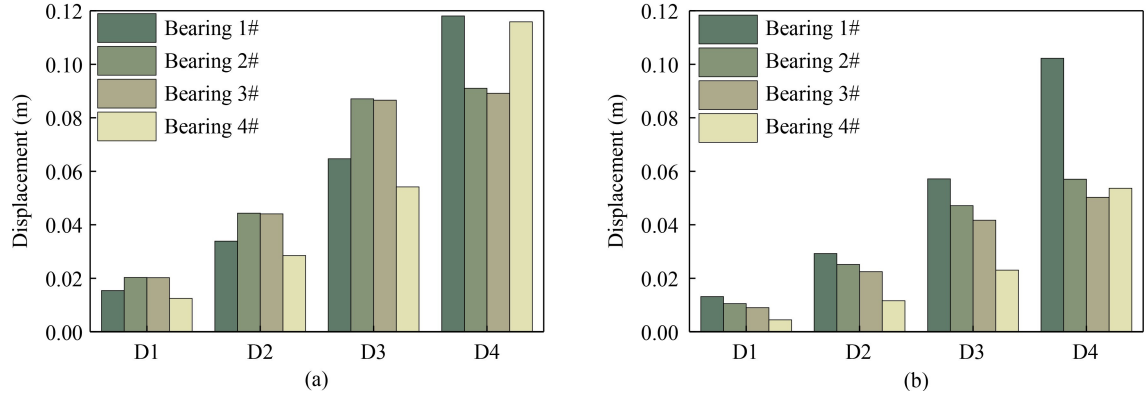

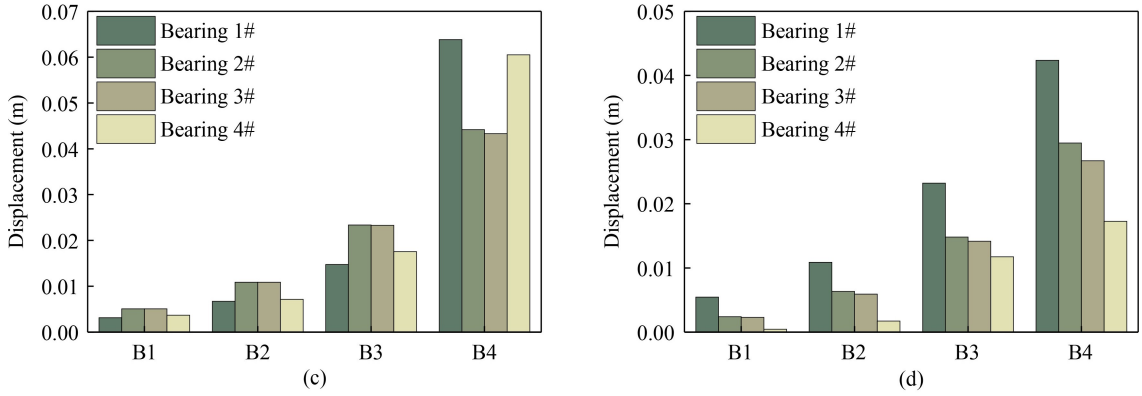

Fig. 11 Comparative study of bearing displacements induced by impulsive versus non-impulsive seismic records: (a) transverse components for impulsive records; (b) longitudinal components for impulsive records; (c) transverse components for non-impulsive records; (d) longitudinal components for non-impulsive records.

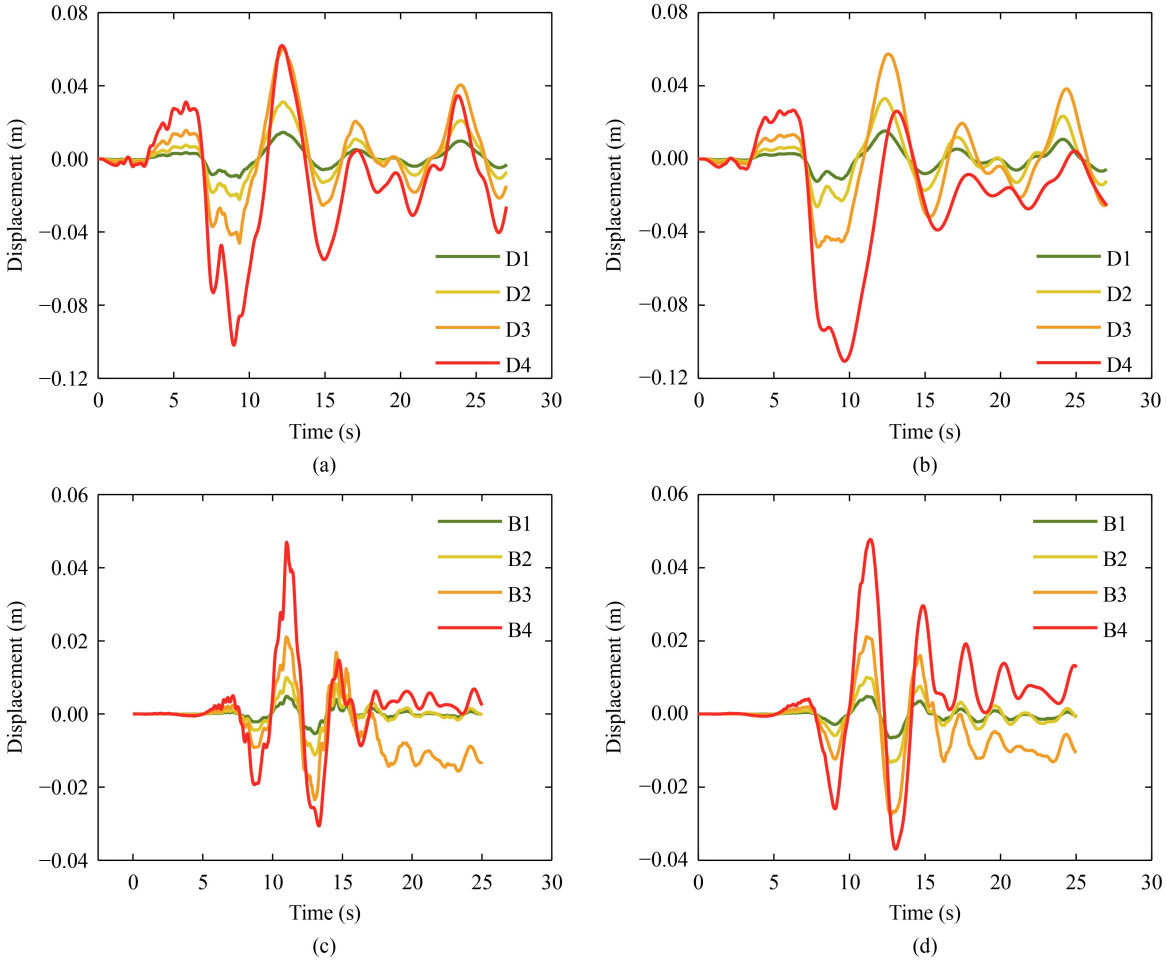

Fig. 12 Comparative study of time-history responses at the main tower top induced by impulsive versus non-impulsive seismic records: (a) longitudinal components for impulsive records; (b) transverse components for impulsive records; (c) longitudinal components for non-impulsive records; (d) transverse components for non-impulsive records.

displacement, a finding that is consistent with the conclusions drawn in the previous section.

As shown in Figs. 12(c) and 12(d), the longitudinal and transverse displacements of the tower top show little variation across the different conditions under non-impulsive ground motions. Overall, the displacements induced by non-impulsive earthquakes are significantly smaller than those from impulsive ones. For example, under the D4 condition, the peak longitudinal and transverse displacements are 0.10 and 0.11 m, respectively. In contrast, under the B4 condition, the corresponding peaks are only 0.047 and 0.05 m.

In summary, the analyses indicate that the intensity of near-fault impulsive earthquakes significantly exceeds that of non-impulsive earthquakes in their effects on bridge components. Therefore, it is imperative to conduct a thorough analysis of bridge members subjected to near-fault impulsive seismic events to ensure their structural integrity and safety.

3.3 Collapse mechanism of cable-stayed bridge under strong seismic actions

Based on nonlinear time-history analysis, this study identifies the typical damage progression sequence in cable-stayed bridges under seismic action: initial damage typically occurs in connecting components such as tower bearings and restrainers, manifesting as bearing slippage, shear deformation, or yielding of restrainers; as seismic intensity escalates, the cable system exhibits abnormal force fluctuations or local slackening, triggering redistribution of internal forces; subsequently, the connections between the main girder and cross beams or the girder root regions enter a state of localized yielding; ultimately, the formation of plastic hinges at the tower bases results in a significant increase in structural residual displacement, raising the risk of global instability and collapse.

To investigate the seismic collapse mechanism of a single-pylon cable-stayed bridge, the ground motion intensity was scaled to a PGA of 12.5 m/s^2. Four critical time instants (t = 10.00, 13.00, 16.00, and 19.00 s) were selected for detailed analysis. The observations indicate that collapse was initiated by damage at the base of the main tower and the top of the adjacent pier 2#, which triggered a redistribution of loads throughout the structure. Subsequently, the main girder fractured under the combined action of seismic and gravitational forces, ultimately leading to a global collapse. For clarity, Fig. 13 illustrates this progressive collapse process, focusing on the pylon and pier 2#.

As depicted in Fig. 13, the structural collapse initiates at t = 10.00 s with initial damage at the base of the main tower under seismic action, although the structure remains globally stable at this stage. By t = 13.00 s, the failure of the tower base triggers a comprehensive redistribution of loads throughout the bridge. This leads to the fracture of the main girder under combined gravity and seismic forces, which in turn weakens the support provided by pier 1# to the girder. Consequently, the load on the main tower surges, causing significant displacement at its base. The failure progresses at t = 16.00 s, as the concrete in the main tower section below its connection with the girder begins to crush and collapse. Ultimately, at t = 19.00 s, the progressive crushing of the

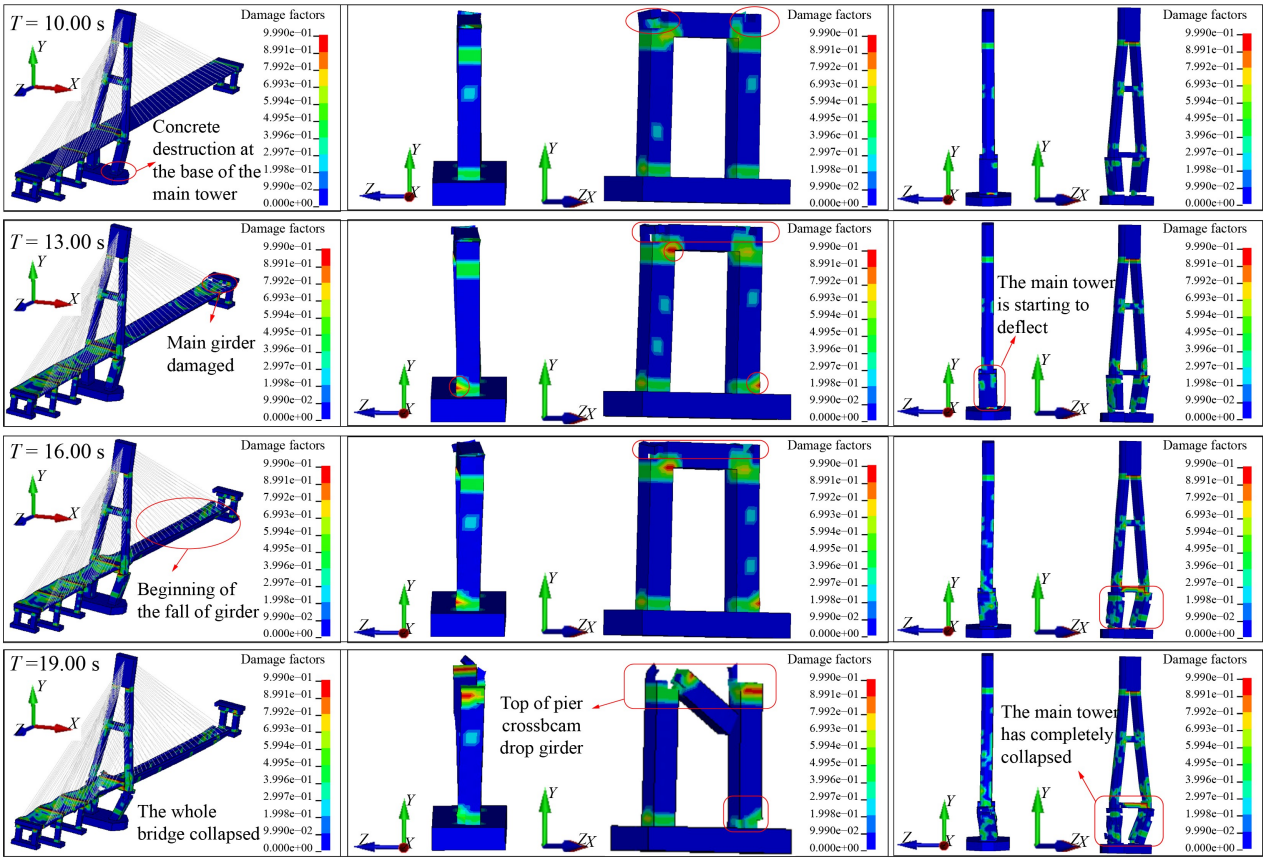

Fig. 13 Collapse process of cable-stayed bridge.

concrete in the lower part of the tower culminates in the complete collapse of the main tower.

As shown in Fig. 13, at t = 10.00 s, pier 2# as a whole remained undamaged. However, localized concrete damage occurred at the connection between the pier and the fixed bearing. By t = 13.00 s, the damage at the top of the pier crossbeam had progressed, with the damage factor at some locations reaching 99%. As time progressed to t = 19.00 s, the severe concrete damage in the pier crossbeam ultimately led to beam falling, resulting in the complete collapse of the pier.

Based on nonlinear time-history analysis results, this study analysis how damage to different components affects bridge function recovery after earthquakes. For example, bearing damage typically shows as slippage or shear deformation. Repair work can be done while keeping partial traffic flow. Temporary supports and phased construction make this possible. Thus, bearing damage causes relatively controllable operational impact. In contrast, stay cable damage, such as abnormal cable force or local slack, requires different responses. It often needs full traffic closure for systematic inspection and stress adjustment. Replacing one cable involves complex tensioning work and long-term monitoring. This leads to much longer service interruption. Moreover, cable damage may trigger internal force redistribution. This can cause further damage to other components, creating a "chain effect" in repairs. Therefore, seismic design should prioritize stay cable safety. At the same time, quick repair plans should be ready for vulnerable components like bearings. This approach will greatly reduce earthquake impact on bridge operation.

4 Bridge fragility and component recoverability analysis

4.1 Ground motion selection

Due to the absence of strong earthquake records at the bridge site, the calculation of bridge fragility necessitates the selection of ground motions that encompass a broad range of intensities. To address this, and given the high practicality of natural ground motions, this study references the Class II site criteria outlined in China's "Code for Earthquake-Resistant Design of Buildings" (GB50011-2010). Accordingly, 30 sets of near-fault impulsive ground motions from the PEER ground motion database are selected, with fault distances ranging from 0.6 to 54.6 km and peak accelerations varying from 0.07g to 0.60g [44]. It is noteworthy that, in accordance with the established criterion defining near-fault distances as being less than 15 km, a secondary screening of the ground motion data was performed. This rigorous filtering ensures the selected data set exclusively comprises near-fault seismic records. The acceleration response spectrum a of the selected ground motions are illustrated in Fig. 14, while the detailed parameters of the ground motions are summarized in Table 5.

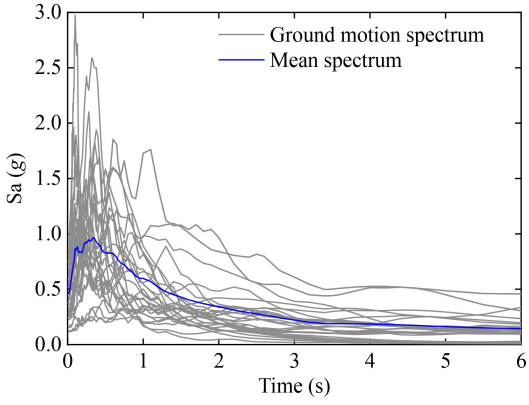

Fig. 14 Acceleration response spectrum for the selected record.

In this study, PGA is used as the IM for fragility analysis. We selected 30 ground motion records from the PEER database. These records were scaled to ten intensity levels from 0.1g to 1.0g, increasing by 0.1g each time. This process used a multi-record scaling approach. For each intensity level, we performed nonlinear time-history analyses on all scaled records. The analysis results provided engineering demand parameters. We compared these parameters with predefined damage state limits. This comparison helped determine when the structure reached different damage levels: slight, moderate, severe, or collapse. We then calculated exceedance probabilities for each damage state at every intensity level. Finally, we fitted a lognormal distribution to these probabilities. This produced the system fragility curves. This method captures the full range of structural behavior. It includes responses from elastic deformation to complete collapse. The approach ensures continuous assessment and provides statistically reliable results.

In fragility calculations, the selection of a ground motion IM is crucial [45]. Currently, PGV and PGA are the primary intensity indices utilized. Ma et al. [46] employed PGA to analyze the fragility of cable-stayed bridges, demonstrating its effectiveness. Furthermore, PGA is particularly suitable for sea-spanning cable-stayed bridges, especially those with shorter spans, it the most appropriate strength index for this type of structure [47]. Therefore, this paper adopts PGA as the strength index to establish the probabilistic demand model for cable-stayed bridges and to derive the fragility curve.

4.2 Selection of damage indicator

The structural DS are categorized as follow [8]: slight damage (DS_1), moderate damage (DS_2), severe damage (DS_3), and complete damage (DS_4). In this study,

Table 5 Ground motion data

Number (RSN)	Grade	Fault distance(km)	Cycle (s)	PGA (*g*)	Number (RSN)	Grade	Fault distance (km)	Cycle (s)	PGA (*g*)
4065	6.0	2.9	1.2	0.32	1520	7.6	18.2	11.1	0.53
4097	6.0	3.0	0.9	0.21	1523	7.6	54.5	8.3	0.07
4098	6.0	3.0	1.3	0.44	1524	7.6	45.2	7.7	0.37
4100	6.0	3.0	1.1	0.62	1525	7.6	54.5	9.5	0.06
4102	6.0	3.6	1.0	0.33	6911	7.0	7.3	9.9	0.45
4103	6.0	4.2	0.7	0.58	6927	7.0	7.1	7.4	0.46
4107	6.0	2.5	1.2	0.60	6928	7.0	25.7	10.6	0.24
4113	6.0	2.9	1.1	0.15	6942	7.0	26.8	8.0	0.20
1491	7.6	7.64	10.4	0.12	6959	7.0	19.5	12.0	0.26
1495	7.6	6.34	–	0.17	6960	7.0	13.6	9.4	0.19
1499	7.6	8.51	–	0.7	6962	7.0	1.5	7.1	0.39
1503	7.6	0.6	5.7	0.79	6966	7.0	22.3	8.8	0.17
1505	7.6	0.3	12.3	0.51	6969	7.0	20.9	9.4	0.18
1510	7.6	0.9	5.0	0.33	6975	7.0	6.1	8.9	0.30
1514	7.6	55.5	9.4	0.08	1605	7.1	6.58	–	0.29

engineering demand parameters for the four DS are defined as follows: for concrete members (including piers, main towers, and main girders), the exterior concrete strain is utilized as the damage indicator [48–50]; for bearings, the relative displacement of the bearings serves as the damage indicator; and for cable-stayed cables, the damage indicator is defined based on the ratio of axial force under seismic loading to axial force under static conditions, as referenced in Wei et al. [51].

When concrete members exceed the elastic ultimate strain, small cracks may develop on their surfaces [48,49]. Accordingly, a DS_1 index is set at 0.0006 [52]. For DS_2, the index is selected as 0.002 [53,54]. The DS_3 index, verified by Cao et al. [55] using the modified Park-Ang damage index, is established at 0.0035. Based on the research of Priestly [56], the DS_4 index is chosen as 0.006, as illustrated in Fig. 15(a). For rubber bearings, the damage limit is defined as 0.1 m [57]. Given that this study focuses on fixed rubber bearings, which possess greater overall stiffness and are more susceptible to damage, four damage indicators are defined: 0.02, 0.04, 0.06, and 0.08 m, as shown in Fig. 15(b). Additionally, the damage indicators for inclined cables are defined as: 0.8, 1.0, 2.0, and 2.5, as depicted in Fig. 15(c).

4.3 Selection of the site of damage

LS-DYNA's explicit dynamic analysis enables clear identification of the most severely damaged bridge components under seismic action. For this purpose, the RSN-4065 ground motion record was scaled to a PGA of 1 m/s^2 and input into the cable-stayed bridge finite element model. As the structural response patterns were found to be consistent across different ground motions, RSN-4065 is presented here as a representative case.

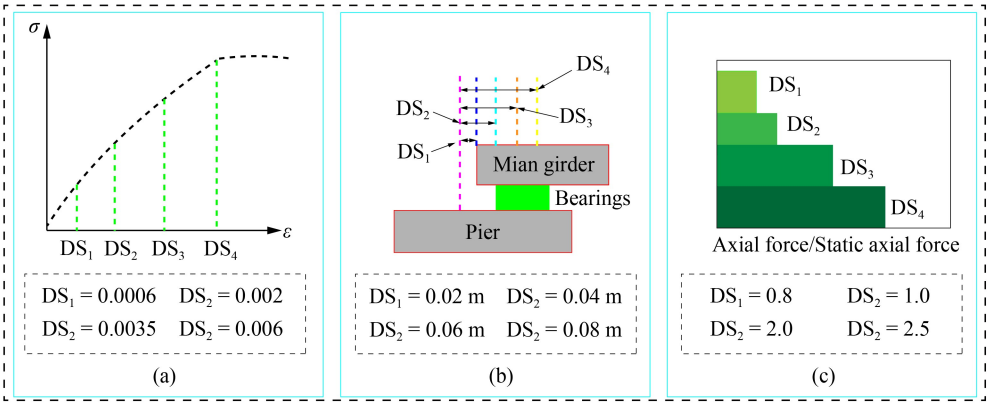

Fig. 15 Fragility indicators: (a) concrete elements damage index; (b) bearings elements damage index; (c) cable elements damage index. (Note: The maximum axial force of the tension cable under self-weight is 450 kN.)

The components exhibiting the most significant responses were selected for detailed analysis, as illustrated in Fig. 16. These include: the base and top of piers 1#–4#; four critical segments of the main tower (Parts 1–4); four key sections of the main girder (Parts 5–8); the longitudinal and transverse directions of bearings 1#–4#; the entire stay cable system; and representative spans along the main girder.

4.4 Fragility analysis of bridge

4.4.1 Theory of fragility analysis

The probability that the seismic demand (D) of a bridge member is greater than or equal to its seismic capacity (C) at a specific intensity of ground motion of IM is called bridge seismic fragility [51]:

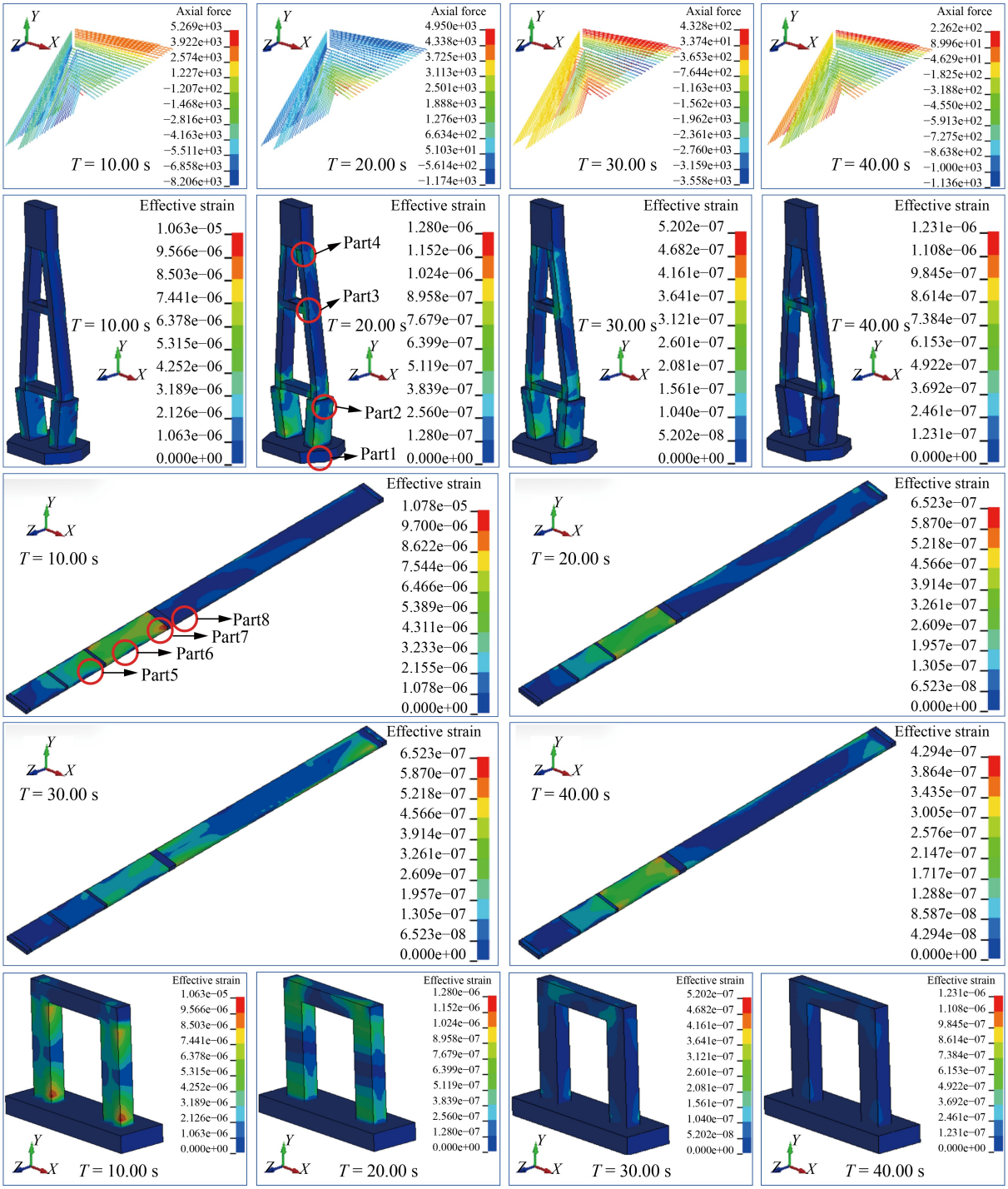

Fig. 16 Primary selection of the damage site.

$$P_{\mathrm{f}} = P[D \geqslant C|IM = x]. \quad (6)$$

Previous studies indicate that the C and D of a bridge structure are typically modeled as following a lognormal distribution in fragility analysis. It is further assumed that the mean value of the structural D (S_{D}) can be represented as an exponential function of the IM. By integrating this assumption with probabilistic structural demand analysis, the relationship between the structural D and the IM can be established, leading to the derivation of a fragility function, as expressed below:

$$P[D \geqslant C|IM] = \Phi\left[\frac{\ln S_D - \ln S_C}{\sqrt{\beta_{D|M}^2 + \beta_C^2}}\right] = \Phi\left[\frac{\ln a + b\ln(IM) - \ln(S_{\mathrm{c}})}{\sqrt{\beta_{D|M}^2 + \beta_C^2}}\right]. \quad (7)$$

Divide the numerator and denominator of Eq. (7) by b at the same time to obtain:

$$P[D \geqslant C|IM] = \Phi\left[\frac{\ln IM - \dfrac{\ln S_{\mathrm{c}} - \ln a}{b}}{\dfrac{\sqrt{\beta_{D|M}^2 + \beta_C^2}}{b}}\right]. \quad (8)$$

The response of the structure is reduced to a quadratic nonlinear fit under logarithmic space with a fragility function:

$$P[D \geqslant C|IM] = \Phi\left[\frac{a\ln(IM)^2 + b\ln(IM) + c - \ln(S_{\mathrm{c}})}{\sqrt{\beta_{D|M}^2 + \beta_C^2}}\right], \quad (9)$$

where S_c is the mean value of C, $\beta_{D|IM}$ is the log standard deviation of the D of the structure, β_C is the log standard deviation of the C of the structure.

The IDA conducted in this study employed a systematic scaling procedure, where the selected ground motion records were amplitude-scaled from an initial PGA of 0.1g up to 1.0g, using a uniform increment of 0.1g. This scaling scheme defined 10 distinct intensity levels for each ground motion, comprehensively capturing structural behavior from the undamaged state to global collapse. The resulting data provide a robust basis for subsequent development of seismic fragility functions.

4.4.2 fragility analysis

Figure 17 shows the maximum strain distribution across nine bridge components under increasing PGA. The data indicate that although most strains remain below the DS_1 threshold, a limited number of components exceed it. Consequently, the following components, which exhibited a minimal damage response, were excluded from the subsequent fragility analysis: the bottom and top of pier 4#, Parts 3 and 4 of the pylon, Part 8 of the main girder, and the mid-span sections of Girders 1 to 4.

Figure 17 illustrates that the damage probabilities for all key components of the main tower, main girder, and piers increase consistently with escalating PGA levels. The seismic fragility results further reveal pronounced heterogeneity in component performance across different DS. Notably, substantial variations in damage probability are observed among components subjected to the same PGA level. A case in point is at PGA = 0.7g, where the probabilities for DS_1 to Parts 1–4 are 99.8%, 4.2%,

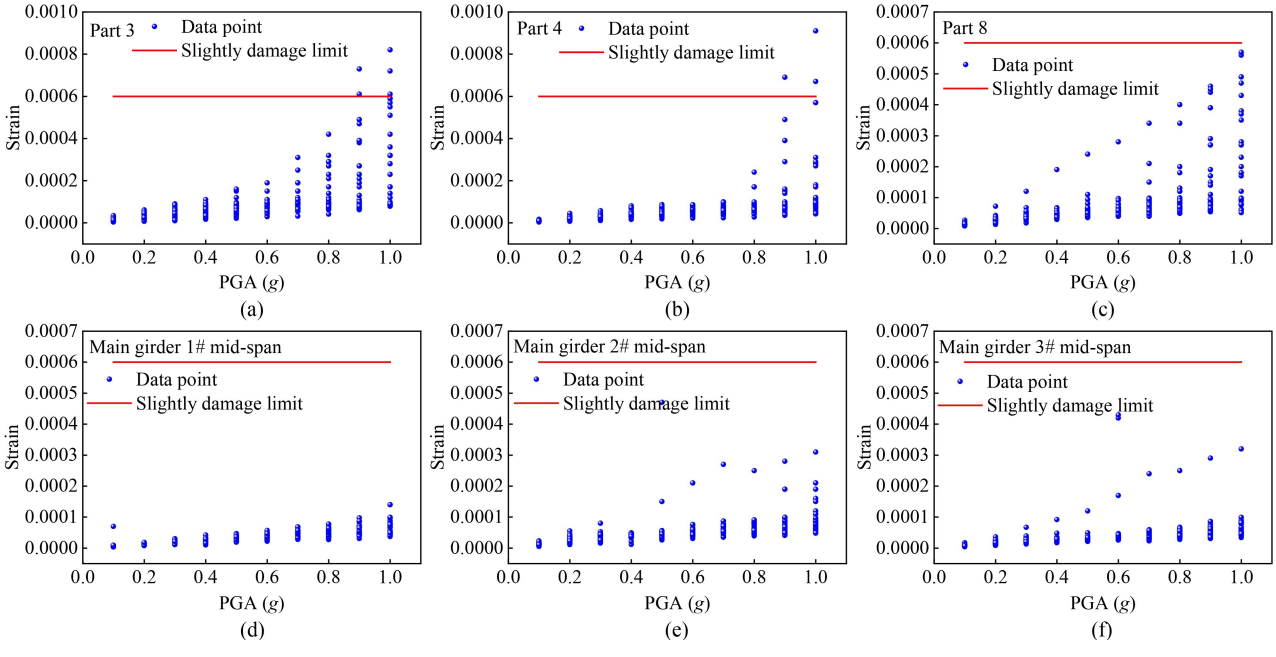

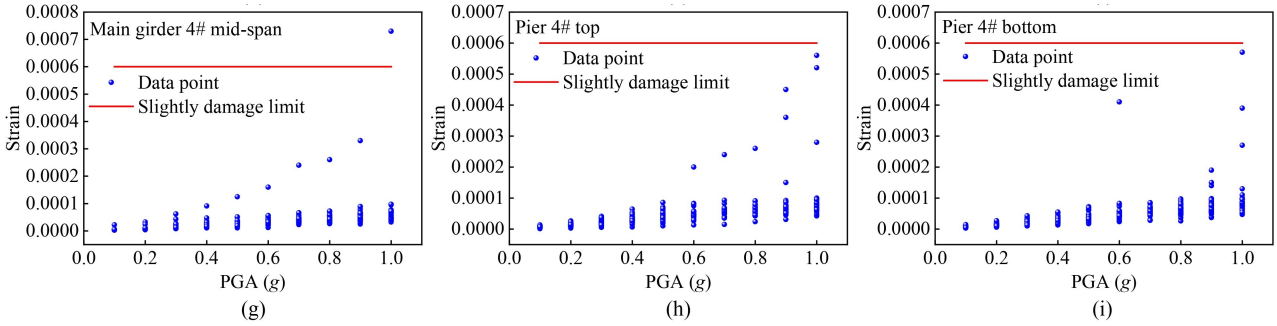

Fig. 17 Components without fragility analysis: (a) part 3; (b) part 4; (c) part 8; (d) main girder 1# mid-span; (e) main girder 2# mid-span; (f) main girder 3# mid-span; (g) main girder 4# mid-span; (h) pier 4# top; (i) pier 4# bottom.

14.3%, and 88.6%, respectively. This finding underscores that the damage probability at the main tower base (Part 1) is substantially higher than that of other tower and girder components.

In addition, the damage probability of pier 2# and pier 3# in each state is similar, and both are much larger than the damage probability of pier 1#, for example, with PGA = 0.7*g*, the probability of DS_1 to the top of the pier 1#–pier 3# is 0.6%, 96.4%, 95.5%; the probability of DS_1 to the bottom of the pier of pier 1#–pier 3# is 1%, 98.8%, 98.4%; the analysis demonstrates that the damage probability at the bottom of the pier is greater than that at the top. It is worth noting that, since the rubber bearings are connected to the main girder and pier in a cemented way, the energy of the main tower under ground motion will be transferred to the middle piers (pier 2#, pier 3#) through the main girder, which makes the damage curve of the middle piers grows significantly within the interval of PGA of 0.4*g*–1.0*g*.

It is noteworthy that damage probabilities for all components remain negligible across the four DS until the PGA reaches 0.5*g*. This indicates that the bridge's substantial structural stiffness and overall stability enable it to effectively withstand *D*s below this intensity threshold. However, once the ground motion intensity exceeds this level, the main tower demonstrates particular vulnerability, exhibiting a rapid increase in damage probability under strong near-fault effects. Owing to the integral connection between the main tower and the girder, progressive damage in the tower directly influences the girder's response, leading to a corresponding increase in the girder's damage probability as the tower damage progresses.

The bearing as the connecting member of the main girder and pier, is most significantly affected by the earthquake, as can be seen from Fig. 18, the magnitude of the probability of damage in the transverse and longitudinal direction of the bearing and the pattern of change are similar, in addition, the probability of DS_1 of bearing 1# transverse at PGA < 0.4*g* is greater than that of the other bearings, whereas the longitudinal direction is smaller than that of the other bearings, for example, with PGA = 0.1*g*, the probability of DS_1 of bearings 1#–4# transverse is respectively: 25.7%, 4.5%, 2.89%, and 0.6%; and in the longitudinal direction, they are: 3.7%, 14.5%, 12.0%, and 15.6%, respectively.

A comparison with Fig. 18 reveals that when PGA ⩽ 0.4*g*, the damage probability of the pier in each damage state is significantly lower than that of the bearing. This indicates that under low-intensity seismic conditions, the bearings preferentially dissipate seismic energy, thereby providing protection to other bridge components. However, as PGA increases, the intermediate pier experiences severe near-fault seismic effects. Due to the inherent flexibility of rubber bearings, whose deformation develops gradually without abrupt changes, and the rigid body characteristics of the pier, the damage probability of the intermediate pier under high-intensity shaking ultimately exceeds that of the corresponding bearing in each damage state.

Consistent with previous research findings indicating that stay cables generally remain elastic under seismic action, Fig. 19 demonstrates relatively low damage probabilities for the diagonal cables across all DS. For instance, at PGA = 1.0*g*, the damage probabilities progress as follows: 93.3% (slight), 85.3% (moderate), 36.8% (extensive), and 21.7% (complete). This progressive damage pattern confirms the excellent seismic performance of the stay cable system in this bridge type, with a significantly higher probability of sustaining only repairable damage rather than progressing to complete failure.

4.5 Component recoverability analysis of bridge

4.5.1 Theory of recoverability

The principle of structural recoverability is defined as the probability that a structure can be restored to its intact seismic performance level following damage incurred during an earthquake [58]. In this context, residual *C* ratio curves are employed to characterize the damage intervals of the structure during IDA. These curves represent the *C* of a structure at various DS, including intact, slightly damaged, moderately damaged, severely damaged, and completely damaged, thereby illustrating the evolution of

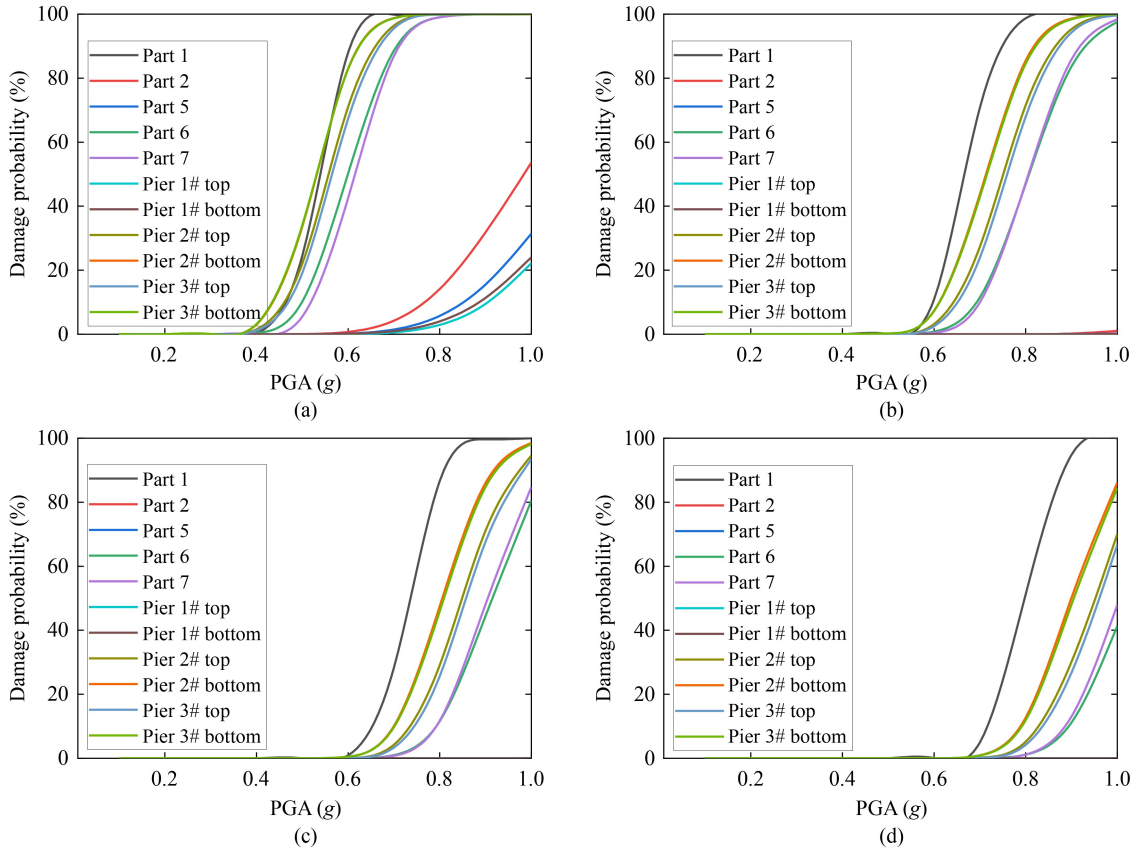

Fig. 18 Main tower, main girder, and pier fragility curves: (a) DS_1; (b) DS_2; (c) DS_3; (d) DS_4.

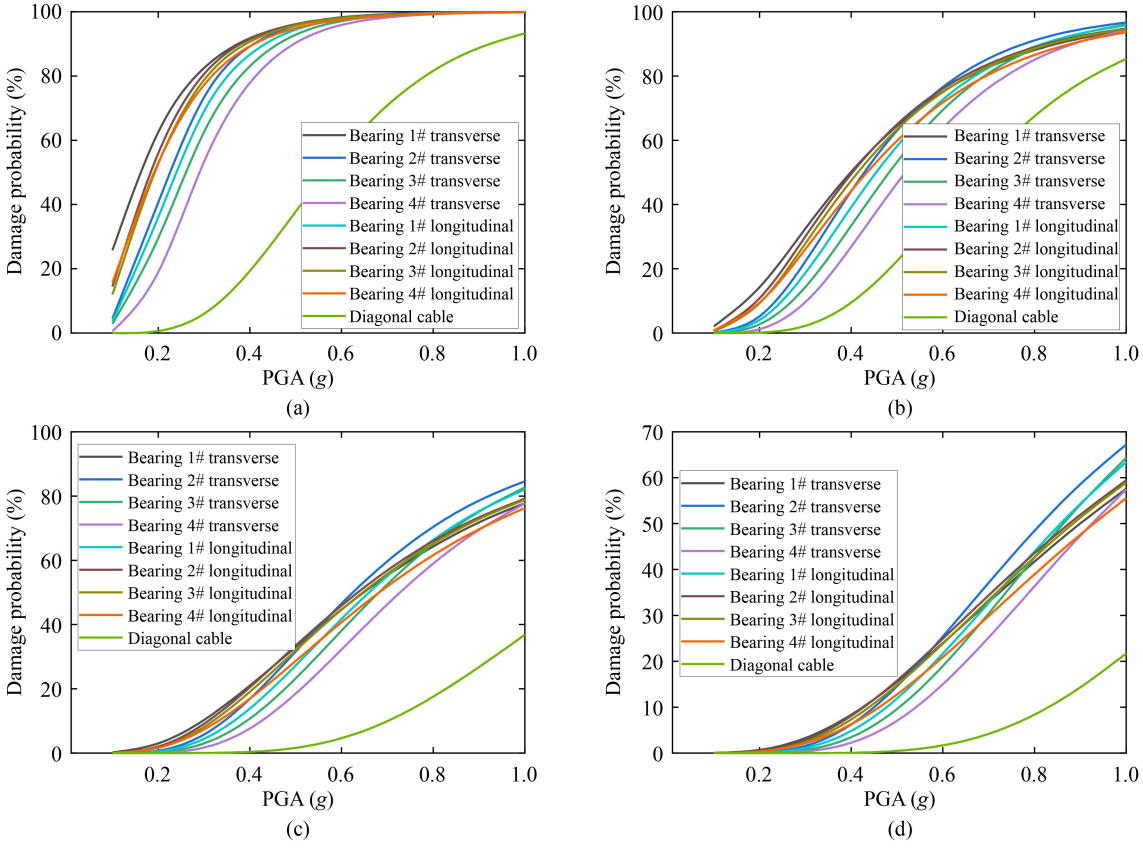

Fig. 19 bearings, diagonal cable fragility curves: (a) DS_1; (b) DS_2; (c) DS_3; (d) DS_4.

the structure's C as damage progresses:

$$C(D)=\frac{M_{IMD}}{Q_{DI}}, \tag{10}$$

where $C(D)$ is the residual ratio of C for the case of structural damage value D, M_{IMD} is the residual amount of C for the case of structural damage value D, Q_{DI} is the design seismic effect.

The stage seismic recoverability index I_{D_i} of the structure is proposed: the ratio of the residual to the ultimate C of its own C within the range of different damage stages is the residual C ratio within a certain damage level interval, and its quantitative expression:

$$I_{D_i}=\int_{D_i}^{D_{i+1}}\frac{C(D)\,\mathrm{d}(D)}{D_{i+1}-D_i}, \tag{11}$$

where D_{i+1} and D_i are the interval limits for the size of the neighboring damage degree, respectively.

Based on the research method of Wu et al. [58], this paper proposes a recoverable model of bridge members under seismic action in the following steps:

Step 1: Utilize PGA as the horizontal coordinate and the member response as the vertical coordinate to perform a nonlinear fit, deriving the fitting equation.

Step 2: Substitute the component's DS_4 index into the fitting equation obtained in Step 1 to determine the corresponding PGA at DS_4.

Step 3: Equally divide the component DS_4 index into 20 response values. (Note that increasing the number of response values at this stage will enhance the accuracy of the final results.)

Step 4: Sequentially input the 20 response values from Step 3 into the fitting equation to obtain the corresponding PGA.

Step 5: Subtract the PGAs obtained in Step 4 from the DS_4 PGA of the member obtained in Step 2. This will yield the PGAs at which each response value must reach DS_4.

Step 6: Compute the ratio $C(D)$ for each response value by dividing the PGA at full damage (obtained in Step 5) by the DS_4 PGA of the member from Step 2.

Step 7: By dividing the 20 response values from Step 3 to the DS_4 value obtain D.

Step 8: Perform a nonlinear fit using the ratios $C(D)$ from Step 6 as the vertical coordinate and the DS_4 indicator D from Step 7 as the horizontal coordinate to derive the fitted equation.

Step 9: Calculate the ratios of DS_1 indicator, DS_2 indicator, DS_3 indicator, and DS_4 indicator relative to the DS_4 indicator of the component. Use these ratios to derive the intact, slight, moderate, and DS_3 intervals for critical parts of the member.

Step 10: Derive the recoverable probability for each damage interval from the equation established in Step 9, and conduct a recoverability analysis.

4.5.2 Component recoverability analysis

Based on the previously established fragility curves for key bridge components, the most vulnerable section from each component type was selected for subsequent restorability analysis. These representative sections include: Part 1 of the main tower, Part 7 of the main girder, the base of pier 2#, and the transverse direction of the bearing at pier 1#. Since the diagonal cables demonstrated negligible damage across all intensity levels, they were excluded from the restorability assessment.

The PGA is used as the horizontal coordinate, and the responses of the selected critical parts of the four parts are used as the vertical coordinate, resulting in the fitted equations shown in Fig. 20.

The 4 parts stage damage intervals are derived from Step 9 and are shown in Table 6.

After dividing the stage damage intervals of each part, after calculating the stage seismic resilience index according to the previous steps, the stage seismic resilience residual ratio curves are plotted and the stage resilience indexes are shown on the graphs, and the stage seismic resilience residual ratio curves of each key part are shown in Fig. 21.

Figure 21 demonstrates that all key components exhibit high seismic recoverability indices within the no-damage range: 0.823 for Part 1 (main tower), 0.775 for Part 7 (main girder), 0.770 for pier 2#, and 0.883 for bearing 1#. These values indicate substantial seismic resilience capacity prior to reaching the DS_1 threshold. As seismic intensity increases and components enter the DS_1 range, their recoverability indices decrease significantly. The pier system experiences the most pronounced reduction of 0.488, resulting in a final index of 0.282. This suggests that while post-earthquake recovery remains possible for slightly damaged components, the likelihood of successful restoration is considerably diminished.

When the components enter the medium damage interval, except for the bearing, the recoverability index of each system is less than 0.15, which indicates that these components can be recovered after the earthquake with great difficulty, and need to be artificially reinforced and repaired.

When the components enter into the DS_3 interval, the recoverability indexes from the main tower system to the bearing system are 0.064, 0.082, 0.023, 0.134, respectively; there is basically no seismic reserve capacity in the systems, and then the structural safety testing must be carried out as soon as possible, and the unsafe components should be strengthened or rebuilt to ensure the safety of the bridge structure. Furthermore, Comparing the recoverability indexes of the four systems,

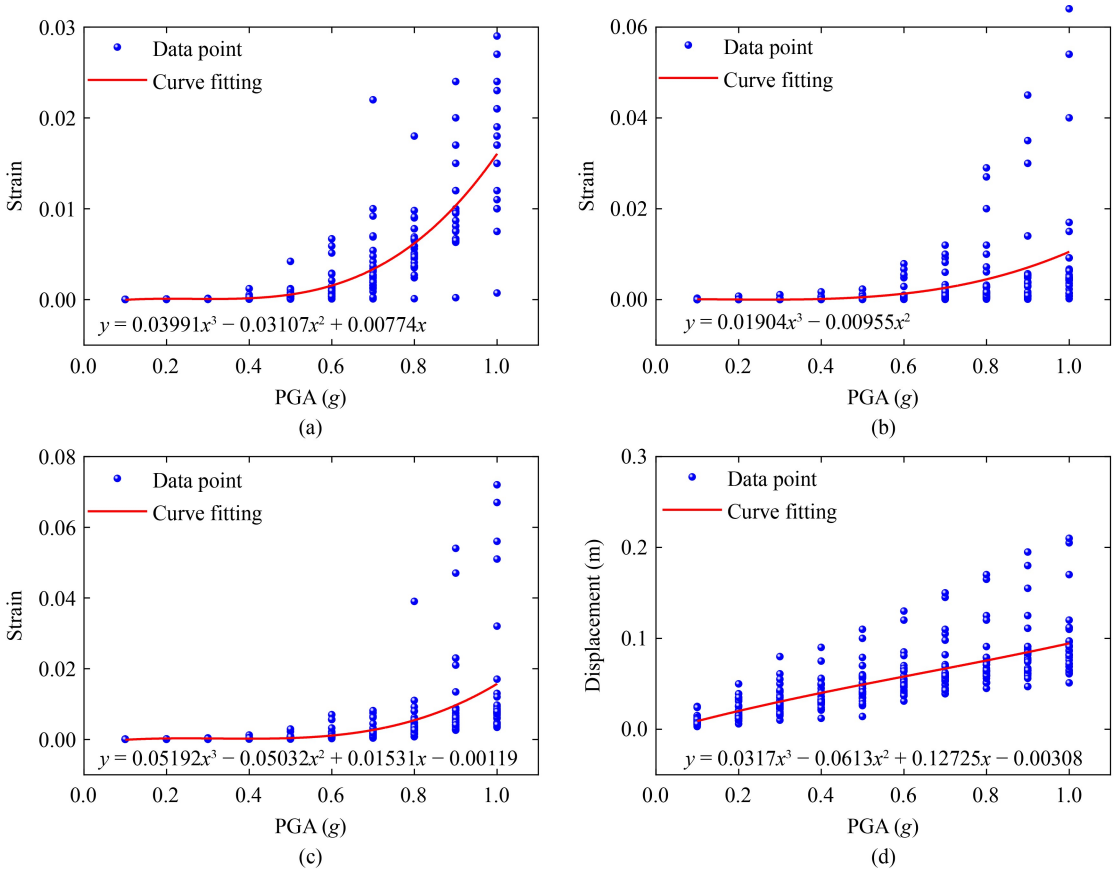

Fig. 20 Ground motion-response value fitting curve: (a) part 1; (b) part 7; (c) pier 2# bottom; (d) bearing 1# transverse.

Table 6 Critical area stage damage classification intervals

Part	Undamage	Slight damage	Moderate damage	Heavy damage	Complete damage
Part 1	0–0.1	0.1–0.333	0.333–0.58	0.58–1	> 1
Part 7	0–0.1	0.1–0.333	0.333–0.58	0.58–1	> 1
Pier 2#	0–0.1	0.1–0.333	0.333–0.58	0.58–1	> 1
Bearing 1#	0–0.25	0.25–0.5	0.5–0.75	0.75–1	> 1

it is found that the bearing system has the strongest recoverability after the earthquake, the main tower system and the pier system are second, and the main girder system is the weakest.

5 Conclusions

This study systematically investigates the seismic performance and post-earthquake recoverability of a single-tower cable-stayed bridge through finite element modeling, nonlinear dynamic analysis, and fragility assessment. The key findings are as follows.

1) Site amplification effects are significant. The site conditions amplify PGA at the surface and modify the acceleration time-history. The amplification exhibits a non-monotonic "increase–decrease–increase" trend with depth, with Soil Layer 2 showing the most pronounced increase.

2) Near-fault impulsive motions govern the D. For identical PGA levels, impulsive ground motions induce substantially greater component damage than non-impulsive motions. The transverse response consistently exceeds the longitudinal response. Under extreme shaking, collapse initiates at the tower base and adjacent abutment, followed by redistribution of internal forces and subsequent girder failure, leading to global collapse.

3) Component vulnerability evolves with shaking intensity. At lower intensity (PGA $\leqslant 0.4g$), bearings act as primary fuses, sustaining initial damage with comparable probabilities in both directions, while the rigid tower–girder connection limits damage to critical load-bearing members. At higher intensity (PGA $> 0.4g$), the tower base becomes the dominant failure location, with its rapidly increasing damage probability driving failure progression in abutments and girders.

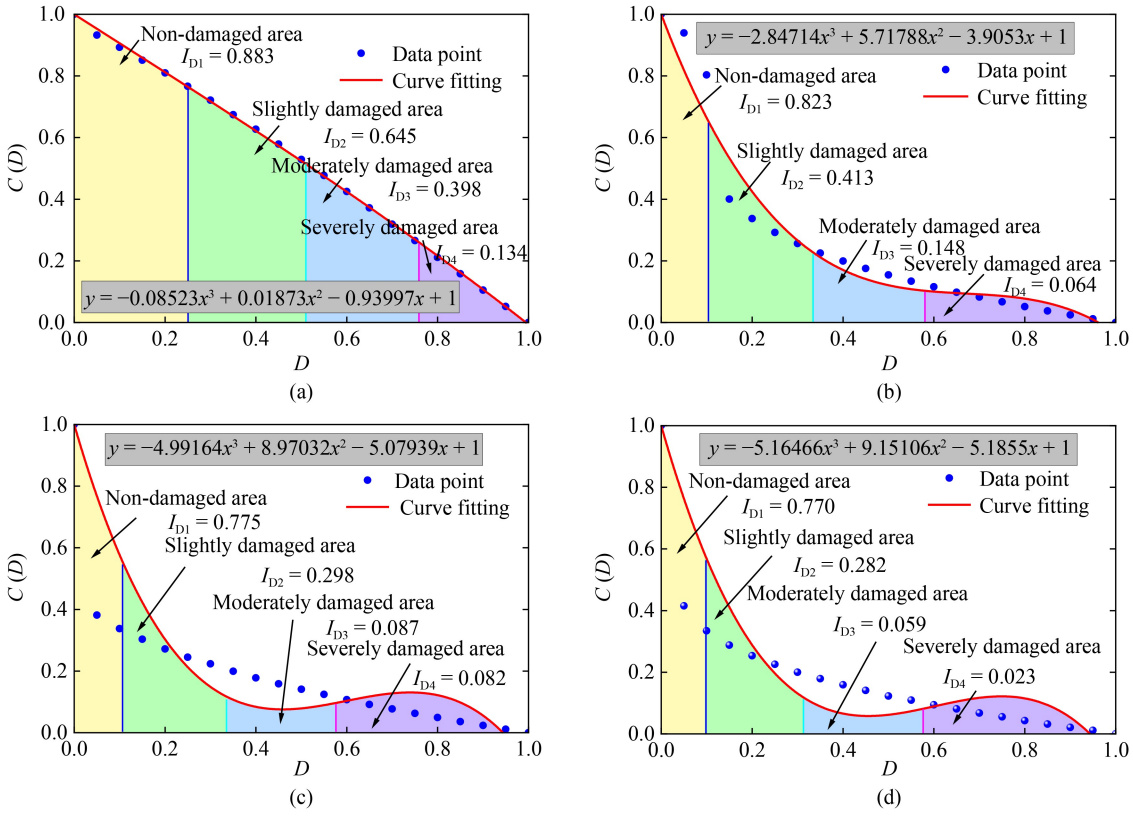

Fig. 21 Stage *C* residual ratio curve: (a) bearing 1# transverse; (b) part 1; (c) part 7; (d) pier 2# bottom.

4) Recoverability varies across components. The bearing system shows the greatest restoration potential, followed by the tower and pier systems, while the girder system exhibits the poorest recoverability, implying higher repair difficulty and cost.

In summary, this study establishes an integrated analytical framework for seismic assessment of cable-stayed bridges, encompassing dynamic response analysis, vulnerability identification, fragility evaluation, and recoverability assessment. The proposed methodology provides a reference for performance-based seismic design and resilience enhancement of cable-stayed bridges.

Acknowledgements This work was joint supported by Key Research and Development Program of Sichuan Provincial Science and Technology Plan (No. 2024YFTX0037), Sichuan Science and Technology Program (No. 2024NSFSC0932), National Natural Science Foundation of China (Grant No. 52008047). Their supports are gratefully acknowledged.

Competing interests The authors declare that they have no competing interests.

References

1. Jiao C, Wang H, Yan B, Wei B, Hu Z, Zheng X, Fang R, Wu R. Impact of the structural system type on the seismic fragility of a multi-tower cable-stayed bridge. Structure and Infrastructure Engineering, 2024: 1–15
2. Zheng S, Shi X, Jia H, Zhao C, Qu H, Shi X. Seismic response analysis of long-span and asymmetrical suspension bridges subjected to near-fault ground motion. Engineering Failure Analysis, 2020, 115: 104615
3. Zheng W, Tan P, Liu Y, Wang H, Chen H. Multi-stage superelastic variable stiffness pendulum isolation system for seismic response control of bridges under near-fault earthquakes. Structural Control and Health Monitoring, 2022, 29(12): e3114
4. Xie W, Sun L. Experimental and numerical investigations on transverse seismic responses of soil-cable-stayed-bridge system subjected to transverse near-fault ground motions. Engineering Structures, 2021, 226: 111361
5. Yi J, Zhou J, Ye X. Seismic evaluation of cable-stayed bridges considering bearing uplift. Soil Dynamics and Earthquake Engineering, 2020, 133: 106102
6. Li C, Li H, Hao H, Bi K, Chen B. Seismic fragility analyses of sea-crossing cable-stayed bridges subjected to multi-support ground motions on offshore sites. Engineering Structures, 2018, 165: 441–456
7. Zeng C, Jiang H, Bai X, Song G. Study on the multi-criteria seismic mitigation optimization of a single pylon cable-stayed bridge across strike-slip fault rupture zones. Engineering Structures, 2023, 275: 115228
8. Li S, Zhang F, Wang J, Alam M, Zhang J. Seismic responses of super-span cable-stayed bridges induced by ground motions in different sites relative to fault rupture considering soil-structure interaction. Soil Dynamics and Earthquake Engineering, 2017,

101: 295–310
9. Chen G, Liu Y, Beer M. Identification of near-fault multi-pulse ground motion. Applied Mathematical Modelling, 2023, 117: 609–624
10. Ma X, Bao C, Doh S, Lu H, Zhang L, Ma X, He Y. Dynamic response analysis of story-adding structure with isolation technique subjected to near-fault pulse-like ground motions. Physics and Chemistry of the Earth Parts A/B/C, 2021, 121: 102957
11. Guo J, Gu Y, Wu W, Chu S, Dang X. Seismic fragility assessment of cable-stayed bridges crossing fault rupture zones. Buildings, 2022, 12(7): 1045
12. Franchini A, Sebastian W, D'Ayala D. Surrogate-based fragility analysis and probabilistic optimisation of cable-stayed bridges subject to seismic loads. Engineering Structures, 2022, 256: 113949
13. Variyavwala J, Gondaliya K, Desai A, Farsangi E. Seismic fragility estimation of cable-stayed bridges with various pylon shapes considering soil-pile interaction. Bulletin of Earthquake Engineering, 2023, 21(7): 3647–3671
14. Zhong J, Xu W, Wei K. Quantifying site-response effect of spatial variability earthquake on seismic failure mode of long-span sea-crossing cable-stayed bridges. Ocean Engineering, 2023, 281: 114839
15. Jia H, Liu Z, Xu L, Bai H, Bi K, Zhang C, Zheng S. Dynamic response analyses of long-span cable-stayed bridges subjected to pulse-type ground motions. Soil Dynamics and Earthquake Engineering, 2023, 164: 107591
16. Jia Y, Xin L, Yang D, Pei M, Zhao L, Huang Z. Seismic behavior analysis of long-span cable-stayed bridge under bi-directional near-fault ground motions. Structures, 2024, 64: 106512
17. Gao L, Liu Z, Dai F, Chen J. Response analysis of a long-span cable-stayed bridge with ultra-high piles subjected to near-fault ground motions considering deep-water, sedimentation, local site, and wave-passage effect. Advances in Bridge Engineering, 2024, 5(1): 34
18. Hu R, Yang M, Meng D, Cucuzza R, Domaneschi M. Robustness investigation of horizontal bidirectional hybrid damping system applied to long-span bridges under near-fault pulse-like earthquakes. Soil Dynamics and Earthquake Engineering, 2024, 184: 108803
19. Guan Z, You H, Li J. An effective lateral earthquake-resisting system for long-span cable-stayed bridges against near-fault earthquakes. Engineering Structures, 2019, 196: 109345
20. Xu L, Jiang Z, Zhang G, Wen J, Han Q, Du X. Endurance time analysis for seismic response of cable-stayed bridge under near-fault pulse-like ground motion. Journal of Vibration Shock, 2025, 44(16): 172–184
21. Yi J. Modeling and analysis of cable vibrations in cable-stayed bridges under near-fault ground motions. Engineering Structures, 2023, 277: 115443
22. Yang D, Liu J, Yu R, Chen G. Unified framework for stochastic dynamic responses and system reliability analysis of long-span cable-stayed bridges under near-fault ground motions. Engineering Structures, 2025, 322: 119061
23. Lin K, Xu Y, Lu X, Guan Z, Li J. Digital twin-based collapse fragility assessment of a long-span cable-stayed bridge under strong earthquakes. Automation in Construction, 2021, 123: 103547
24. Zheng Y, Wu H, You X, Xie H. Model updating-based dynamic collapse analysis of a RC cable-stayed bridge under earthquakes. Structures, 2022, 43: 1100–1113
25. Scattarreggia N, Salomone R, Moratti M, Malomo D, Pinho R, Calvi G. Collapse analysis of the multi-span reinforced concrete arch bridge of Caprigliola, Italy. Engineering Structures, 2022, 251: 113375
26. Scattarreggia N, Galik W, Calvi P, Moratti M, Orgnoni A, Pinho R. Analytical and numerical analysis of the torsional response of the multi-cell deck of a collapsed cable-stayed bridge. Engineering Structures, 2022, 265: 114412
27. Qian J, Zheng Y, Dong Y, Wu H, Guo H, Zhang J. Sustainability and resilience of steel-shape memory alloy reinforced concrete bridge under compound earthquakes and functional deterioration within entire life-cycle. Engineering Structures, 2022, 271: 114937
28. Chandrasekaran S, Banerjee S. Retrofit optimization for resilience enhancement of bridges under multihazard scenario. Journal of Structural Engineering, 2016, 142(8): C4015012
29. Badroddin M, Chen Z. Lifetime resilience measurement of river-crossing bridges with scour countermeasures under multiple hazards. Journal of Engineering Mechanics, 2021, 147(9): 04021058
30. Yang S, Mavroeidis G, Ucak A, Tsopelas P. Effect of ground motion filtering on the dynamic response of a seismically isolated bridge with and without fault crossing considerations. Soil Dynamics and Earthquake Engineering, 2017, 92: 183–191
31. Zhang F, Li S, Zhao T, Wang J. Seismic cable restrainer design method to control the large-displacement response for multi-span simply supported bridges crossing fault rupture zones. Soil Dynamics and Earthquake Engineering, 2021, 149: 106881
32. Agalianos A, Sieber M, Anastasopoulos I. Cost-effective analysis technique for the design of bridges against strike-slip faulting. Earthquake Engineering & Structural Dynamics, 2020, 49(11): 1137–1157
33. Hu M, Han Q, Wen J, Bai Y. Seismic failure of multi-span simply supported RC slab-on-grider bridge in 2008 Wenchuan earthquake. Engineering Failure Analysis, 2019, 95: 140–153
34. Jia H Y, Wu W, You G, Yang L, Peng Q, Zheng S. Damage analysis of long-span continuous beam bridge under strong earthquakes. Journal of Southwest Jiaotong University, 2023, 58(6): 1423–1431 (in Chinese)
35. Simo J C, Ju J W. Strain-and stress-based continuum damage models—I. Formulation. International Journal of Solids and Structures, 1987, 23(7): 821–840
36. Murray Y. Users Manual for LS-DYNA Concrete Material Model 159, 2007
37. Zhou Q, Qi L. Analysis and comparison of 5 different common anti-explosion concrete material models of LS-DYNA software. Concrete, 2019, 11: 43–49 (in Chinese)
38. Fan W, Xu X, Zhang Z, Shao X. Performance and sensitivity analysis of UHPFRC-strengthened bridge columns subjected to vehicle collisions. Engineering Structures, 2018, 173: 251–268
39. Fan W, Yuan W C. Numerical simulation and analytical modeling of pile-supported structures subjected to ship collisions including

soil–structure interaction. Ocean Engineering, 2014, 91: 11–27
40. Xia C X, Liu C G. Analysis of seismic response characteristics of cable-stayed bridges under near-fault multi-pulse ground motion. Bridge Construction, 2018, 48(3): 29–34 (in Chinese)
41. Bi K, Hao H. Numerical simulation of pounding damage to bridge structures under spatially varying ground motions. Engineering Structures, 2013, 46: 62–76
42. Hashash Y, Park D. Non-linear one-dimensional seismic ground motion propagation in the Mississippi embayment. Engineering Geology, 2001, 62(1-3): 185–206
43. Hashash Y, Park D. Viscous damping formulation and high frequency motion propagation in non-linear site response analysis. Soil Dynamics and Earthquake Engineering, 2002, 22(7): 611–624
44. Shafieezadeh A, Ramanathan K, Padgett J, DesRoches R. Fractional order intensity measures for probabilistic seismic demand modeling applied to highway bridges. Earthquake Engineering & Structural Dynamics, 2012, 41(3): 391–409
45. Zhong J, Pang Y, Jeon J, DesRoches R, Yuan W. Seismic fragility assessment of long-span cable-stayed bridges in China. Advances in Structural Engineering, 2016, 19(11): 1797–1812
46. Ma K, Zhong J, Feng R, Yuan W. Investigation of ground-motion spatial variability effects on component and system vulnerability of a floating cable-stayed bridge. Advances in Structural Engineering, 2019, 22(8): 1923–1937
47. Kowalsky M. A displacement-based approach for the seismic design of continuous concrete bridges. Earthquake Engineering & Structural Dynamics, 2002, 31(3): 719–747
48. Priestley M, Calvi G, Kowalsky M, Powell G. Displacement-based seismic design of structures. Earthquake Spectra, 2008, 24(2): 555–557
49. Priestley M, Kowalsky M. Direct displacement-based seismic design of concrete buildings. Bulletin of the New Zealand Society for Earthquake Engineering, 2000, 33(4): 421–444
50. Su J, Dhakal R P, Wang J. Fiber-based damage analysis of reinforced concrete bridge piers. Soil Dynamics and Earthquake Engineering, 2017, 96: 13–34
51. Wei B, Hu Z, He X, Jiang L. System-based probabilistic evaluation of longitudinal seismic control for a cable-stayed bridge with three super-tall towers. Engineering Structures, 2021, 229: 111586
52. Shao G, Jiang L, Chouw N. Experimental investigations of the seismic performance of bridge piers with rounded rectangular cross-sections. Earthquakes and Structures, 2014, 7(4): 463–484
53. Hose Y D, Seible F. Performance Evaluation Database for Concrete Bridge Components and Systems under Simulated Seismic Loads. PEER Technical Report 1999/07. 1999
54. Wang Y, Liu Z, Yang W, Hu Y, Chen Y. Damage index of reinforced concrete members based on the energy dissipation capability degradation. Structural Design of Tall and Special Buildings, 2020, 29(2): e1695
55. Cao S, Jiang L, Wei B. Numerical and experimental investigations on the Park-Ang damage index for high-speed railway bridge piers with flexure failures. Engineering Structures, 2019, 201: 109851
56. Priestley M. Displacement-based seismic assessment of reinforced concrete buildings. Journal of Earthquake Engineering, 1997, 1(1): 157–192
57. Liu BS, Ren XX, Xue B, Wang QH, Lu WS. Experimental study on mechanical behavior of small scale lead rubber bearings. China Civil Engineering Journal, 2022, 55(S1): 112–117 (in Chinese)
58. Wu F, Meng Y, Chen Y, Ji Q, Yang Y, Wu Z. Analysis of seismic fragility and recoverability of long-span cable-stayed bridge. Journal of Southwest Jiaotong University, 2020, 55(01): 126–133 (in Chinese)